UNIVERSITÉ DE GENÈVE
INSTITUT DES SCIENCES DE L'ENVIRONNEMENT

Complementary Certificate in Geomatics

Chlorophyll-a estimates in the Nuup Kangerlua using remote sensing data and its potential use for greenhouse gases sea-air fluxes analysis

---

Thesis presented by
Paul Gabriel Molineaux

Under the direction of
Prof. Gregory Giuliani, Head of the Digital Earth Unit [GRID – Geneva] & Senior Lecturer in Earth Observations [UNIGE]

University of Geneva – Faculty of Social Sciences

2023

Copyright

Acknowledgement

First of all, I would like to warmly thank my thesis director, Prof. Gregory Giuliani, for his continuous support and help which allowed me to work with confidence and efficiency. I would also like to thank Prof. Daniel Frank McGinnis and PhD Cesar Ordõnez for paving the way for me to work on greenhouse gases in the Arctic. Leila Hottinger and Caroline Guenat also provided me a more than welcome help by working as master students on greenhouse gases in the Arctic before me. They produced the original greenhouse gases dataset used in this thesis.

Finally, I give a special thanks to Quinten Vanhellemont from the Royal Belgian Institute of Natural Sciences for the development of ACOLITE and his countless answers on forums about atmospheric corrections and chlorophyll estimates.

Abstract

Fjords play an important role in the carbon cycle as they are believed to be strong carbon dioxide (CO_2) uptake places and emitters of methane (CH_4). Net primary production (NPP), with chlorophyll-*a* (Chl-*a*) as proxy, also plays a role in the carbon cycle as CO_2 is consumed in photosynthesis and CH_4 produced through the depletion of organic matter. This study aims at providing remote sensing estimates of Chl-*a* to better understand the GHGs fluxes occurring in fjords, with the case study of the Nuup Kangerlua. Three Chl-*a* retrieval algorithms have been compared to select the most adapted for the study region. To produce estimates with a sufficiently high spatial resolution for this fjord, it is necessary to use Sentinel-2A (S2A) scenes. Then results have compared with Sentinel-3A (S3A) scenes as the Ocean and Land Color Instrument (OLCI) is providing ready-to-use Chl-*a* estimates. The data produced with this remote sensing study has been added to a greenhouse gases (GHGs) dataset to analyze the fluxes of CO_2 and CH_4 in Nuup Kangerlua. The analysis indicates that the study region is an important sink of CO_2 with an average of -17.65 (±17.42) [mmol m^{-2} d^{-1}]. It corresponds to an annual uptake of approximatively -77 [g C m^{-2} y^{-1}]. It is an emitter of CH_4 with an average of 14.67 (±19.47) [µmol m^{-2} d^{-1}] during the period of measurements. It corresponds to annual emissions of approximatively 0.06 [g C m^{-2} y^{-1}]. Glacial meltwater inputs are a driver of the strong CO_2 no main driver of the CH_4 fluxes was identified.

Table of contents

List of figures

List of tables

Acronym List

AMAP	Arctic Monitoring and Assessment Programme
CDOM	Coloured Dissolved Organic Matter
Chl-*a*	Chlorophyll-*a*
CH_4	Methane
CO_2	Carbon Dioxide
GHGs	Greenhouse gases
MERIS	Medium Resolution Imaging Spectrometer
MODIS	Moderate Resolution Imaging Spectroradiometer
MSI	MultiSpectral Instrument
NAP	Non-Algal Particular matter
NPP	Net Primary Production
OLCI	Ocean and Land Color Instrument
SeaWIFs	Sea-viewing Wide Field-of-view Sensor
S2A L1C	Sentinel 2-A Level 1C
S3A	Sentinel 3-A

1. Introduction

The Arctic Ocean plays an important role in the carbon cycle as it is believed to be a net sink of CO_2 and a net source of CH_4 (Parmentier et al. 2013; Weber et al. 2019). More specifically, fjords tend to be hotspots of these sources and sinks (Bonaglia et al. 2022; Meire et al. 2015). However, the scale of the carbon cycle in the Arctic is still subject to uncertainties (McGuire et al. 2009; Saunois et al. 2020). These uncertainties are enhanced by the fast warming of the region (McGuire et al. 2009). In addition, the remoteness of the Arctic makes the collection of *in-situ* data complex and expensive. It emphasizes the opportunity that remote sensing data represents.

The decrease in sea-ice extent is responsible for an increase of up to 30% of net primary production (NPP) in the Arctic Ocean between 1998 and 2009 (Arrigo et van Dijken 2011). It could enhance the uptake of CO_2 of the ocean (Meire et al. 2015; Ruiz-Halpern et al. 2010) and the emissions of CH_4 through the depletion of organic matter by methanogenic *Archaea* in anaerobic environments (Saunois et al. 2020). However, the changes in NPP and the carbon fluxes vary both spatially and seasonally. Arrigo et Van Dijken (2015) found that a portion of Baffin Bay and the Greenlandic outflow shelf show no increase of NPP over the period 1998-2012, whereas the Beaufort Sea and Barents Sea show a positive trend. In addition, the complex hydrology of fjords is upset by the increase in meltwater inputs due to global warming and it could render fjords less productive (Holding et al. 2019).

This study aims to add remote sensing data of chlorophyll-a (Chl-*a*) to a greenhouse gases (GHGs) fluxes dataset in Nuup Kangerlua, on the south-west coast of Greenland. Before addressing the problematic of this work, it is necessary to review the challenges that remote sensing of Chl-*a* represents in the Arctic Ocean.

1.1 Remote Sensing Chlorophyll-a estimation in the Arctic Ocean

1.1.1 Challenges

Estimating Chl-*a* in the Arctic Ocean using ocean colour remote sensing presents serious challenges. High and persistent cloud cover and large river runoffs make arctic waters different from the rest of the world's oceans (Arrigo et al. 2011; Carmack et al. 2006). Freshwater inputs from river runoffs tends to increase the presence of coloured dissolved organic matter (CDOM) which absorbs wavelengths strongly in the blue and much less in the green, as Chl-*a*. It can contribute more than Chl-*a* in the absorption of these wavelengths (Matsuoka et al. 2009) and thus lead to overestimate Chl-*a* when using algorithms based on these wavelengths to estimate Chl-*a* concentration (Lewis et al. 2016).

In addition, Chl-*a* is generally used as a proxy of NPP or to calculate it through algorithms. However, the large solar zenith angles at high latitudes tends to make phytoplankton increase their Chl-*a* concentration to absorb enough light. As a result, the phytoplankton absorbs less light per unit of Chl-*a*, thus leading to an overestimation of NPP (Arrigo et al. 2011).

Ocean colour remote sensing of Chl-*a* is based on the surface upwelling radiance, occulting the processes occurring deep in the mixed layer (Martin et al., 2010). If the subsurface Chl-*a* maximum develops itself deep in the mixed layer, it can lead to underestimate the Chl-*a* concentration in the water column (Arrigo et al. 2011).

According to Arrigo et al. (2011) and using Sea-viewing Wide Field-of-view Sensor (SeaWiFS), all these factors tend to compensate each other over the entire Arctic Ocean. However, the presence of CDOM is stronger near freshwater inputs (Lund-Hansen et al. 2010) and can thus increase the error in a fjord system.

1.1.2 The Nuup Kangerlua

The Nuup Kangerlua is located on the western coast of Greenland and Nuuk, the capital of Greenland, is situated at the mouth of the fjord. It is subject to the challenges presented above, but higher variability of optic properties can occur in Greenlandic fjords (Mascarenhas et Zielinski 2019). According to Murray et al. (2015) in this fjord, 15-32% of photons are absorbed by Chl-*a*, 7-8% by non-algal particular matter (NAP) and 6-13% by CDOM. The fjord presents high variability within itself due to meltwater inputs (Mascarenhas et Zielinski 2019). Fjords aren't necessarily hotspot of NPP. Indeed, meltwater is turbid, limiting the light available in the water layer, forcing phytoplankton to stay away from the nitracline. In addition, meltwater is freshwater and thus have a high buoyancy. It makes the water column very stratified and limits upwelling (Holding et al. 2019). Sills present at the entrance of most fjords also slow the mixing of water at the seabed (Straneo et Cenedese 2015). Nonetheless, the Nuup Kangerlua is believed to be a large sink of CO_2 due to its NPP, and meltwater inputs (Meire et al. 2015). On the other hand, the hydrology of fjords reduces the oxygen content deep in the water layer, enhancing methane production. The Nuup Kangerlua should thus be an important emitter of CH_4 (Bonaglia et al. 2022).

1.1.3 Atmospheric corrections and Chlorophyll-*a* algorithms

In this work, Sentinel-2A L1C (S2A L1C) scenes are used to estimate Chl-*a*. They offer a resolution of 10 to 20 meters depending on the bands of concern, which is more accurate than the traditional Moderate Resolution Imaging Spectroradiometer (MODIS) or the Sea-viewing Wide Field-of-View Sensor (SeaWIFs) scenes or even the recent Sentinel-3 Ocean and Land Color Instrument (OLCI). However, S2A L1C imagery was designed to be used over land and needs atmospheric corrections to be used over water bodies (Chen et al. 2017; Vanhellemont et Ruddick 2016). The algorithm ACOLITE[1] for atmospheric corrections has shown good performance in the processing of water imagery, even for sediment-rich waters (Maciel et Pedocchi 2022), and was thus used in this work.

Once the scenes have been processed through ACOLITE, it is necessary to use other algorithms to retrieve Chl-*a* estimates. In this work, three methods to retrieve Chl-*a* will be used and compared. Chl-*a* is a proxy of phytoplankton as it is its primary photosynthetic pigment. Blue-green ratio algorithms are used to estimate Chl-*a* as this pigment absorbs more blue and red than green

[1]Natural Sciences.be, https://odnature.naturalsciences.be/remsem/software-and-data/acolite

light. At the same time, the color of ocean water goes from deep blue to green as phytoplankton concentrations increase (O'Reilly et al. 1998). Blue-green ratio thus provides an estimate of the presence of Chl-*a*. The first algorithm for Chl-*a* retrieval used in this work is the ocean chlorophyll (OC3) blue-green ratio algorithm, first developed by O'Reilly et al. (1998) for SeaWIFs but it can be used with Landsat-8 or S2A L1C scenes (Franz et al. 2015; Tehrani, Janalipour, et Babaei 2021; Vanhellemont et Ruddick 2016).

The second algorithm is derived from the first one but adapted for the Arctic region (OC4L) (Cota 2004). To make it work with S2A L1C scenes, one of the original four bands has been dropped as it is not directly available with the MultiSpectral Instrument (MSI), this algorithm will thus be referred as OC3L.

Both these algorithms have the advantage of providing relatively good results while being easy to implement. However, CDOM and NAP can lower the accuracy of these algorithms because they present similar absorption spectrum as Chl-*a*, leading to potential overestimations (Vanhellemont et Ruddick 2016). The potential implications of the change from OC4L to OC3L will be discussed in Chapter 2.3.

The third algorithm is the red-edge algorithm and has been developed by Gons (2002) for the Medium Resolution Imaging Spectrometer (MERIS) but can also be used with S2A L1C imagery (Vanhellemont et Ruddick 2016). It should avoid the overestimation due to CDOM and NAP. However, the natural variability of the absorption coefficient of Chl-*a* can lead to some errors. It has been developed for very high concentration of chlorophyll (3 to 185 [mg m^{-3}] (Gons 2002)) and could thus be inappropriate for a less productive fjord system.

The atmospheric corrections algorithm can also produce uncertainties. Pahlevan et al. (2021) tested 8 methods for atmospheric corrections, including the ACOLITE algorithm. They showed that the median error ranged between 15-30% and 20-30% depending on the dataset used. They further demonstrated that such errors could lead to median error in Chl-*a* remote sensing estimates ranging from 25 to 70%, limiting the use of the results. However, the main drivers of uncertainties are the aerosols which are probably not very present over Greenland and the Nuup Kangerlua as it is a remote place. It is at least the case for central Greenland, which presents lower than average aerosols concentrations (Von Schneidemesser et al. 2009).

Moreover, newly developed techniques using machine learning provide higher accuracy than simple algorithms, but they must be trained with *in-situ* Chl-*a* data, which are not available for this work (Zhu et al. 2022).

Sentinel-3A (S3A) imagery also provide good products for estimating Chl-*a*, with a resolution of 300X300 m^2. Two algorithms are already used in the available products of S3A, one of them being the OC4Me[2]. This algorithm uses four bands, and is a blue-green ratio algorithm as the OC3 and the OC3L. It has the same basis as the algorithms developed by O'Reilly et al. (1998)

[2] Sentinel online, https://sentinel.esa.int/web/sentinel/technical-guides/sentinel-3-olci/level-2/oc4me-chlorophyll

but has been adapted by Morel, Huot, et al. (2007). Altogether, it makes the S3A Chl-*a* estimates a good object of comparison and should provide additional confidence on the S2A L1C Chl-*a* estimates.

1.2 Problematic

In light of the previous introduction and with the aim of adding Chl-*a* estimates to a GHGs fluxes dataset to discuss their coherence in the absence of calibration with *in situ* data, it is first necessary to address the two following questions:

Q1. Between the OC3, the OC3L and the red-edge algorithms, which one is the most appropriate to use with S2A scenes in Nuup Kangerlua?

Q2. How does it compare with the S3A OC4Me algorithm estimates?

After exploring the various Chl-*a* estimates, it will be possible to test them with the GHGs fluxes dataset by answering the following question:

Q3. Do the dissolved concentrations and fluxes of CO_2 and CH_4 vary depending on Chl-*a* estimates?

Whether the answer to **Q3** is positive or negative, it will be useful to analyse other variables present in the dataset to better understand how concentrations and fluxes vary in Nuup Kangerlua. The complex hydrology of a fjord forces different water bodies to coexist with specific physicochemical characteristics. These characteristics will be explored to try to answer the following question:

Q4. Do the dissolved concentrations and fluxes of CO_2 and CH_4 vary depending on the hydrology of the Nuup Kangerlua?

2. Methodology

The methodology used for this work is briefly described in Figure 1. There are two distinct parts, the production of Chl-*a* estimates, and its use on a greenhouse gases dataset. The production of Chl-*a* estimates with S2A scenes took several additional steps in comparison to S3A. The GHGs dataset was originally produced by two master students, Leila Hottinger and Caroline Guenat, and was only slightly adapted and revised for this work (cf. Appendix 3).

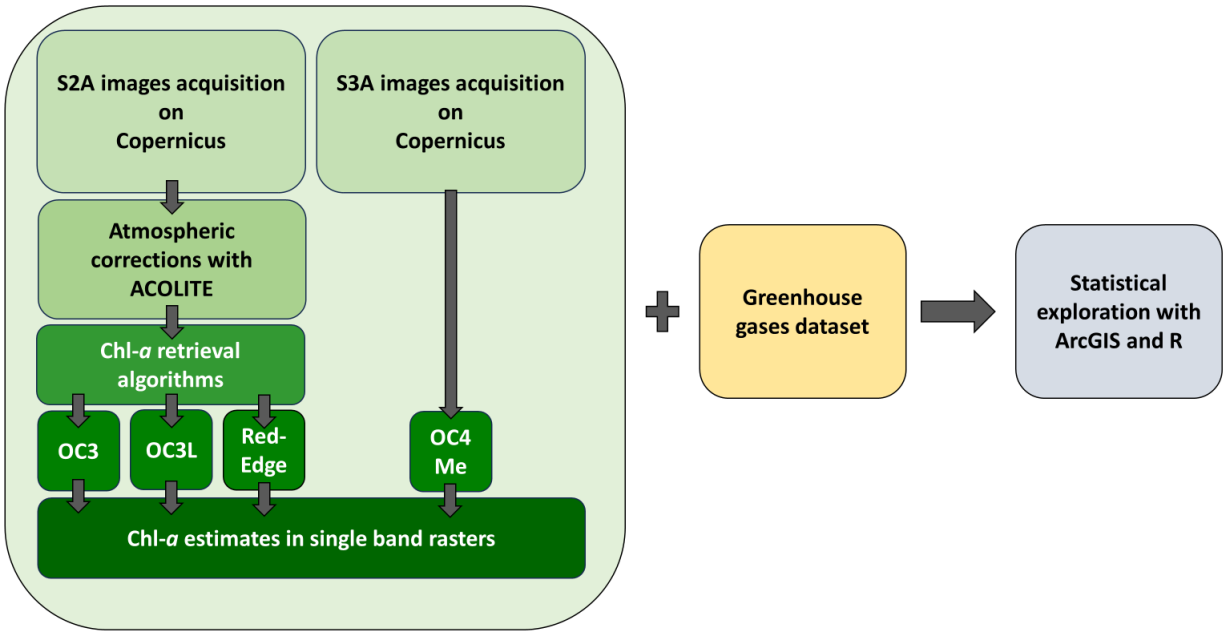

Figure 1. Workflow overview.

2.1 Images acquisition

The satellites images used in this work, both S2A L1C and S3A were retrieved through the Copernicus Browser[3]. The GHGs dataset, which will be described below in Chapter 2.4, has datapoints going from the 24th of June to the 5th of August 2021. After going through the available S2A L1C images between these dates, three dates were selected to make Chl-*a* estimates. The 22nd of June, the 9th of July and the 29th of July 2021 allow to capture most of the evolution during the period of measurements. They are the clearer images and limit the amount of data to process. However, it increases the uncertainty of Chl-*a* estimates for datapoints in between these dates. An additional image from the 31st of August 2021 was downloaded to take a perfectly clear picture of the Nuup Kangerlua at the end of summer.

The area of interest, the Nuup Kangerlua, is more than 200 kilometers long, leading to the need of downloading two images per date for S2A L1C scenes. However, only one S3A image was needed per date. The three S3A images were selected to be as close in time as possible from the S2A L1C scenes and were taken at the following dates: the 22nd of June, the 8th of July, and the 28th of July 2021.

[3] Copernicus, https://dataspace.copernicus.eu/browser/?zoom=3&lat=26&lng=0&themeId=DEFAULT-THEME&visualizationUrl=https%3A%2F%2Fsh.dataspace.copernicus.eu%2Fogc%2Fwms%2Fa91f72b5-f393-4320-bc0f-990129bd9e63&datasetId=S2_L2A_CDAS

2.2 Atmospheric corrections

S3A scenes are already atmospherically corrected for use over water bodies and are thus not concerned by the process described here. S2A L1C scenes are produced for land use and need corrections to be used over water (Chen et al. 2017; Vanhellemont et Ruddick 2016). Several algorithms are available for this purpose, but in this study the ACOLITE[4] algorithm was used as it shows good results in the processing of water imagery (Maciel et Pedocchi 2022).

The ACOLITE algorithm uses the "dark spectrum fitting" approach which has been developed by Vanhellemont et Ruddick (2018). The ACOLITE GUI was used with the parameters rhow_443, rhow_492, rhow_560, chl_oc3 and chl_re_gons. The three first parameters allow to retrieve atmospherically corrected surface reflectance over water for the wavelengths 443, 492 and 560 [ηm]. The chl_oc3 and the chl_re_gons allow to directly retrieve Chl-*a* estimates using the OC3 and the red-edge algorithms, which will be described below in Chapter 2.3. This parametrisation reduces the processing time required.

The outputs of the atmospheric corrections are single band raster layers that can be easily manipulated in ArcGIS pro to make Chl-*a* estimates.

2.3 Chlorophyll-*a* algorithms

2.3.1 OC3 for Sentinel-2A

ACOLITE provides ready-to-use estimates of Chl-*a* using several algorithms. In this work, the classic OC3 (O'Reilly et al. 1998) and the red-edge (Gons 2004) algorithms have been selected. The OC3 is a three bands blue-green ratio algorithm and is similar as the OC3L and OC4Me algorithms described below in Chapter 2.3.2 and 2.3.4, offering a good comparison. On the other hand, the red-edge algorithm (described below in Chapter 2.3.3) is built over different bands and should thus offer more differences.

The OC3 algorithm used by ACOLITE was first adapted by O'Reilly et Werdell (2019) for the Operational Land Imager (OLI) from Landsat-8 and then for the MSI from Sentinel-2 by Pahlevan et al. (2020). It uses the bands of the following centered wavelengths: 442, 492 and 560 [ηm].

It is expressed as (Pahlevan et al. 2020):

$$log_{10}[\text{Chl-}a] = a_0 + \sum_1^n a_n \times [log_{10}(\frac{Max\ R_{rs}(442,492)}{R_{rs}(560)})]^n \qquad \text{(Eq. 1)}$$

Max R_{rs} (442,492) stands for the maximum value between these two bands. Chl-*a* is in [mg m^{-3}]. The constants a_n are described for each algorithm in Table 1.

[4] Natural Sciences.be, https://odnature.naturalsciences.be/remsem/software-and-data/acolite

Table 1. Constants for the different algorithms.

Algorithm	a_0	a_1	a_2/b_1	a_3	a_4
OC3 (Pahlevan et al. 2020)	0.3308	-2.6684	1.5990	0.5525	-1.4876
OC3L (Cota 2004)	-	0.592	-3.607	-	-
OC4Me (Morel et al. 2007)	0.4502748	-3.259491	3.522731	-3.359422	0.949586

2.3.2 OC4L for Sentinel-2A: OC3L

The OC4L algorithm is also a blue-green ratio algorithm. It is a linear algorithm, with constants tuned for arctic waters where high nutrients and low light availability typically lead to highly "packaged" pigments with lower specific absorption (Cota et al. 2003). It has been developed for SeaWIFs by Cota (2004) and uses the same four bands as the OC4Me algorithm described below (cf. Chapter 2.3.4), except for the last band. The four bands in question are of the following centered wavelengths: 443, 490, 510 and 555 (560 for the OC4Me) [ηm].

In this study, the OC4L algorithm has been adapted to work with S2A, becoming an OC3L algorithm. Indeed, S2A does not provide a band of centered wavelength of 510 [ηm] as the bands are wider and the 510 [ηm] band is mostly contained within the 492 [ηm] band of S2A. The maximum absorption of Chl-*a* is around 442.5 [ηm] while the minimum is around 560 [ηm][5], two wavelengths well covered by S2A.

It is expressed as follows (adapted from Cota 2004):

$$log_{10}[\text{Chl-}a] = a_1 + b_1 \times [log_{10}(\frac{Max\ R_{rs}(442,492)}{R_{rs}(560)})] \qquad \text{(Eq. 2)}$$

Max R_{rs} (442,492) stands for the maximum value between these two bands. Chl-*a* is in [mg m^{-3}]. The constants a_n are described for each algorithm in Table 1. The original OC4L is the same with *Max R_{rs} (443,490,510)/R_{rs}(555)* instead of the current *Max R_{rs} (442,492)/R_{rs}(560)*. This change could lead to less precise estimation of Chl-*a* for pixels where $R_{rs}(510)$ is high, typically in Chl-*a* -rich waters, because the ratio $R_{rs}(510)/R_{rs}(560)$ is mostly used for high Chl-*a* concentrations (O'Reilly et al. 2000). Nonetheless, it is a good object of comparison as it has two clear differences, with the OC4Me, using one less band, and with the OC3, being tuned for arctic waters.

2.3.3 Red-edge for Sentinel-2A

The third algorithm is the red-edge algorithm and has been developed by Gons (2002) for MERIS but can also be used with S2A L1C imagery (Vanhellemont et Ruddick 2016). It uses bands of centered wavelengths 664, 704 and 780 [ηm]. It should avoid the overestimation due to CDOM and NAP as these particles absorb in the blues. However, it has been developed for

[5] Sentinel online, https://sentinel.esa.int/web/sentinel/user-guides/sentinel-3-olci/resolutions/radiometric

high concentration of Chl-*a* (3 to 185 [mg m^{-3}]) as the reflectance peak around 705 [ηm] is more visible in Chl-*a* -rich waters (Cota et al. 2003; Gons 2004).

ACOLITE allows to produce ready-to-use Chl-*a* estimates using the red-edge algorithm developed by Gons (2002). It uses the following total backscattering coefficient (adapted for S2A from Gons (2004)):

$$b_b = \frac{1.61 \times R_w(780)}{0.082 - 0.6 \times R_w(780)} \quad \text{(Eq. 3)}$$

Where R_w stands for water leaving reflectance for a given wavelength. The backscattering coefficient can then be inserted into the following equation(adapted for S2A from Gons (2004)):

$$[\text{Chl-}a] = \frac{\frac{R_w(704)}{R_w(664)} \times (0.70 + b_b) - 0.40 - b_b^{1.06}}{0.015} \quad \text{(Eq. 4)}$$

Where R_w stands for water leaving reflectance for a given wavelength. Chl-*a* is in [mg m^{-3}]. The number 0.015 was used as the absorption coefficient of Chl-*a* (Royal Belgian Institute of Natural Sciences (RBINS) 2023). Outputs were only produced when surface reflectance at 664 [ηm] were above 0.005 and when the ratio of surface reflectance 704/664 [ηm] was above 0.63 (RBINS, 2023).

2.3.4 OC4Me for Sentinel-3A

S3A scenes directly provide Chl-*a* estimates using the OC4Me algorithm or the neural network algorithm. S3A scenes are used in this work in the purpose of comparison with S2A L1C scenes and the OC4Me is very close in calculations (cf. Eq 1, 2, and 5) from the OC3 and OC3L algorithms and was thus selected. This algorithm uses four bands and is a blue-green ratio algorithm as the OC3 and the OC3L. It has the same basis as the algorithms developed by O'Reilly et al. (1998) and O'Reilly et al. (2000) but has been adapted by Morel et al. (2007) for MERIS which provides bands with similar wavelength as S3A.

The OC4Me algorithm is expressed as (Morel et al. 2007):

$$log_{10}[\text{Chl-}a] = a_0 + \sum_1^n a_n \times [log_{10}(\frac{Max\ R_{rs}(443,490,510)}{R_{rs}(560)})]^n \quad \text{(Eq. 5)}$$

The original OC4Me uses $R_{rs}(555)$ for greens (instead of $R_{rs}(560)$ in Eq. 5) but S3A provides only $R_{rs}(560)$ which is used in their official product under the name OC4Me. *Max R_{rs} (443,490,510)* stands for the maximum value between these three bands. Chl-*a* is in [mg m^{-3}]. The constants a_n are described for each algorithm in Table 1.

2.4 Datasets

The results of the four algorithms described in Chapter 2.3 are four single bands raster layers of Chl-*a* estimates in [mg m^{-3}], for each of the three dates selected in Chapter 2.1. A limit of

100 [mg m^{-3}] was imposed as higher values are highly improbable in Nuup Kangerlua (Meire et al. 2015). The values of each raster were extracted using the coordinates of the samples from the GHGs dataset and added to it. The datapoints go from the 24th of June to the 5th of August 2021. An additional variable was added using the closest Chl-*a* estimates in time from the time of sampling. Samples from the 24th of June to the 30th received the Chl-*a* estimates of the 22nd of June. Samples from the 1st of July to the 19th received the Chl-*a* estimates of the 9th of July. Finally, samples from the 20th of July until the 5th of August received the Chl-*a* estimates of the 29th of July.

The GHGs dataset originally contains 132 samples for 22 variables. The first six variables only give the name, number, date, time, and coordinates of the samples. Then the following five physical parameters are displayed: water temperature [°C], atmospheric pressure [mbar], wind speed [m s^{-1}], air temperature [°C] and depth [m]. Then, eleven chemical parameters are presented: pH, salinity [PSU], dissolved oxygen [% of saturation], dissolved CH_4 [% of saturation], dissolved CO_2 [% of saturation], atmospheric concentration of CH_4 [ppb], atmospheric concentration of CO_2 [ppm], dissolved concentration of CH_4 [ppb], dissolved concentration of CO2 [ppm], CH_4 sea-air fluxes [µmol m^{-2} d^{-1}] and CO_2 sea-air fluxes [mmol m^{-2} d^{-1}]. Appendix 1 describes the acquisition of the data contained in this dataset.

Several samples were removed as specified in Appendix 2 due to mistakes in the sampling such as contamination with respiration.

A CTD (YSI EXO2 Multiparameter Sonde) produced an additional separate dataset. It did a measure every 10 minutes, from the 24th of June until the 6th of August and is composed of 6302 points. It was then combined with the GPS points from the ship. Due to some missing coordinates and the movements of the ship, fewer points can be displayed on a map.

Finally, the depth values were retrieved from the IBCAO database (Jakobsson et al. 2020).

3. Results

3.1 Chlorophyll estimates

To have an overview of the four different algorithms used and be able to compare them in Chapter 4, they will be presented below but only for the 22nd of June 2021. Additional scenes are in the Appendixes and will serve the discussion.

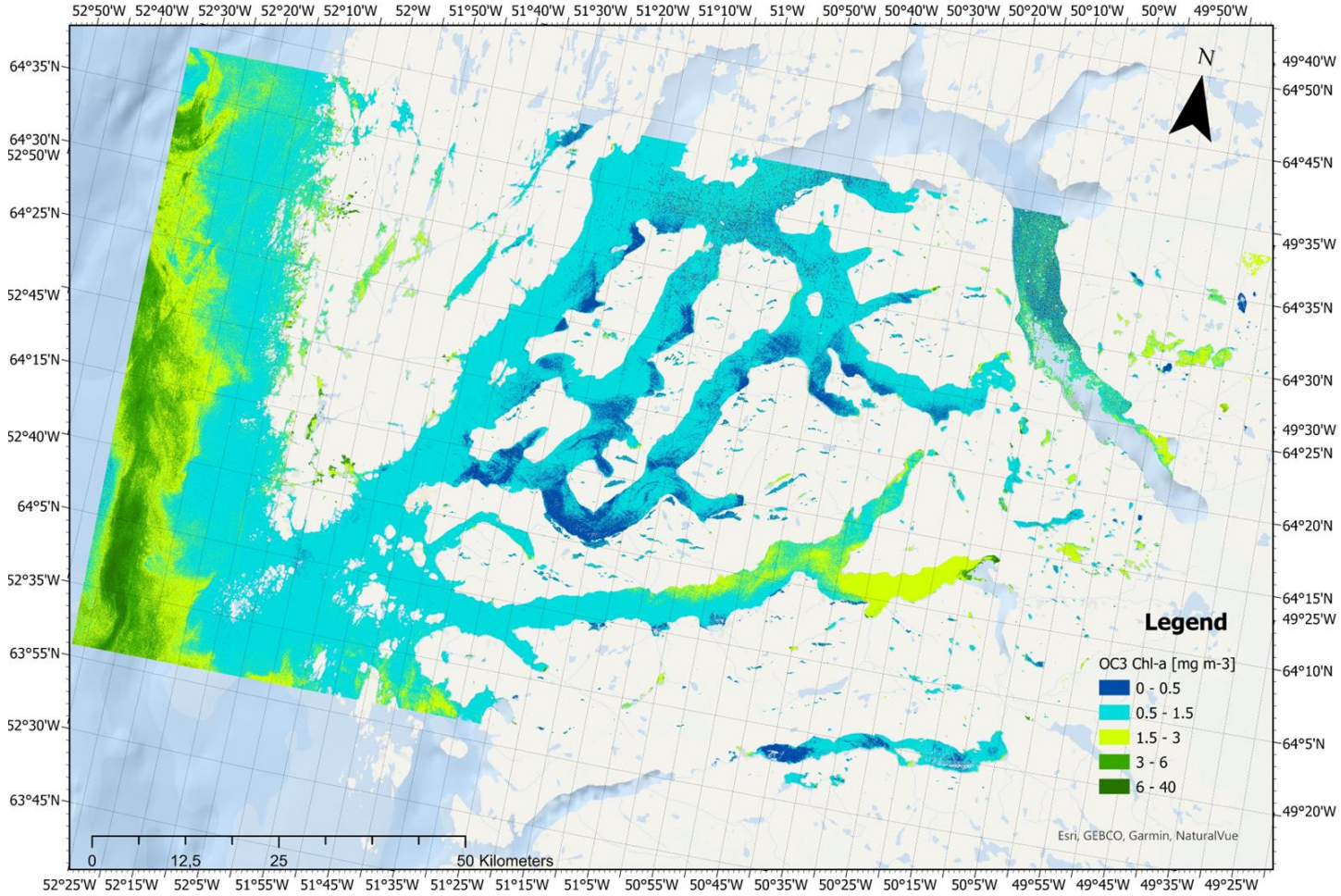

Figure 2. Chl-a estimates in [mg m-3] from the OC3 algorithm (Pahlevan et al. 2020) using S2A L1C scenes from the 22nd of June 2021.

In Figure 2, two inlets present higher Chl-*a* estimates near the glaciers in the east than in the middle of the fjord. Except for these two hotspots, the Chl-*a* concentrations in the fjord are low and well distributed. The highest Chl-*a* estimates are situated offshore of the Western coast of Greenland.

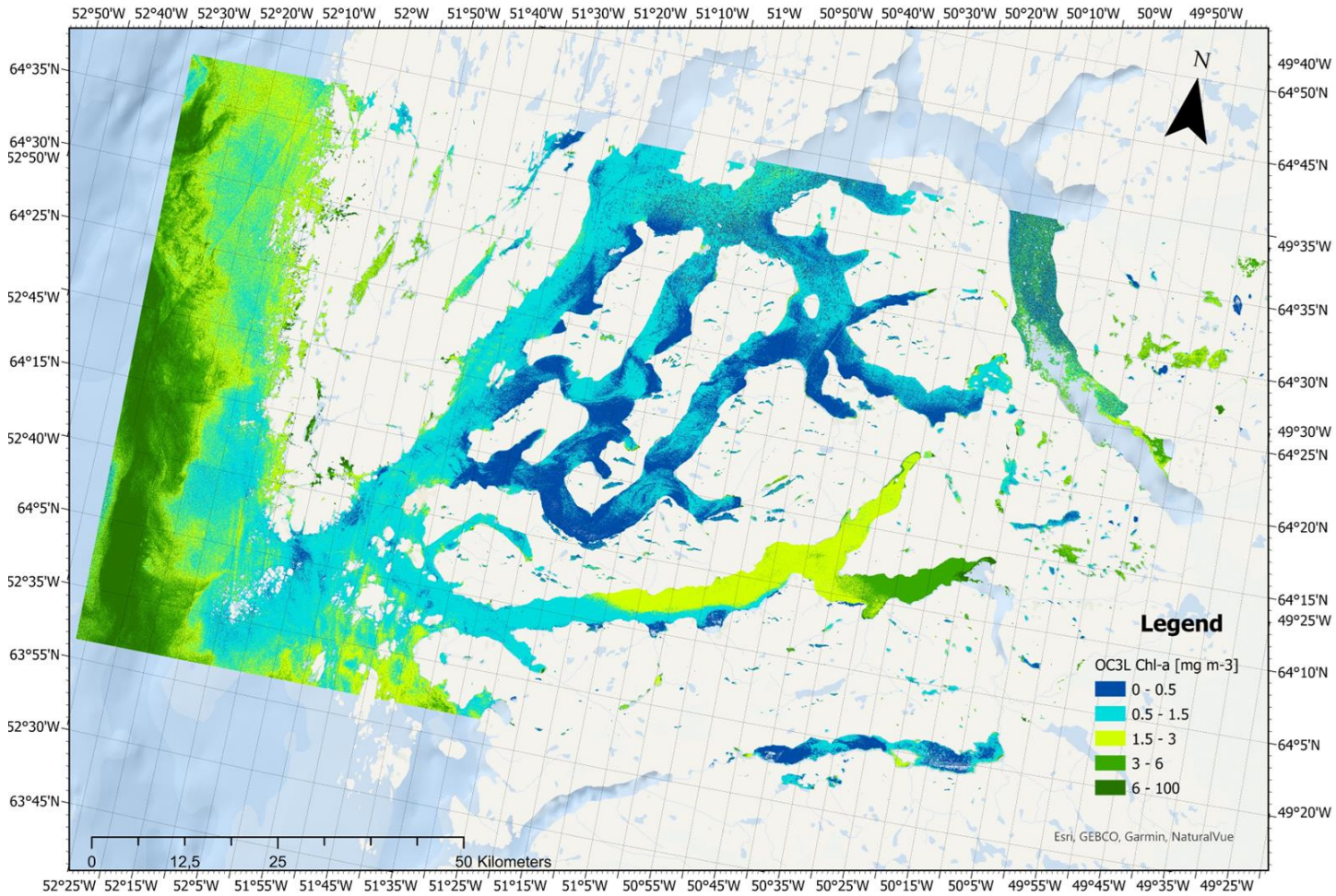

Figure 3. Chl-a estimates in [mg m-3] from the OC3L algorithm (derived from Cota 2004) using S2A L1C scenes from the 22nd of June 2021.

As for Figure 2, two inlets present higher Chl-*a* estimates near the glaciers in the east than in the rest of the fjord (Figure 3). Variations are well visible with the lowest estimates in the middle of the fjord and a marked hotspot in the Southern inlet of the Nuup Kangerlua. The highest Chl-*a* estimates are situated offshore of the Western coast of Greenland.

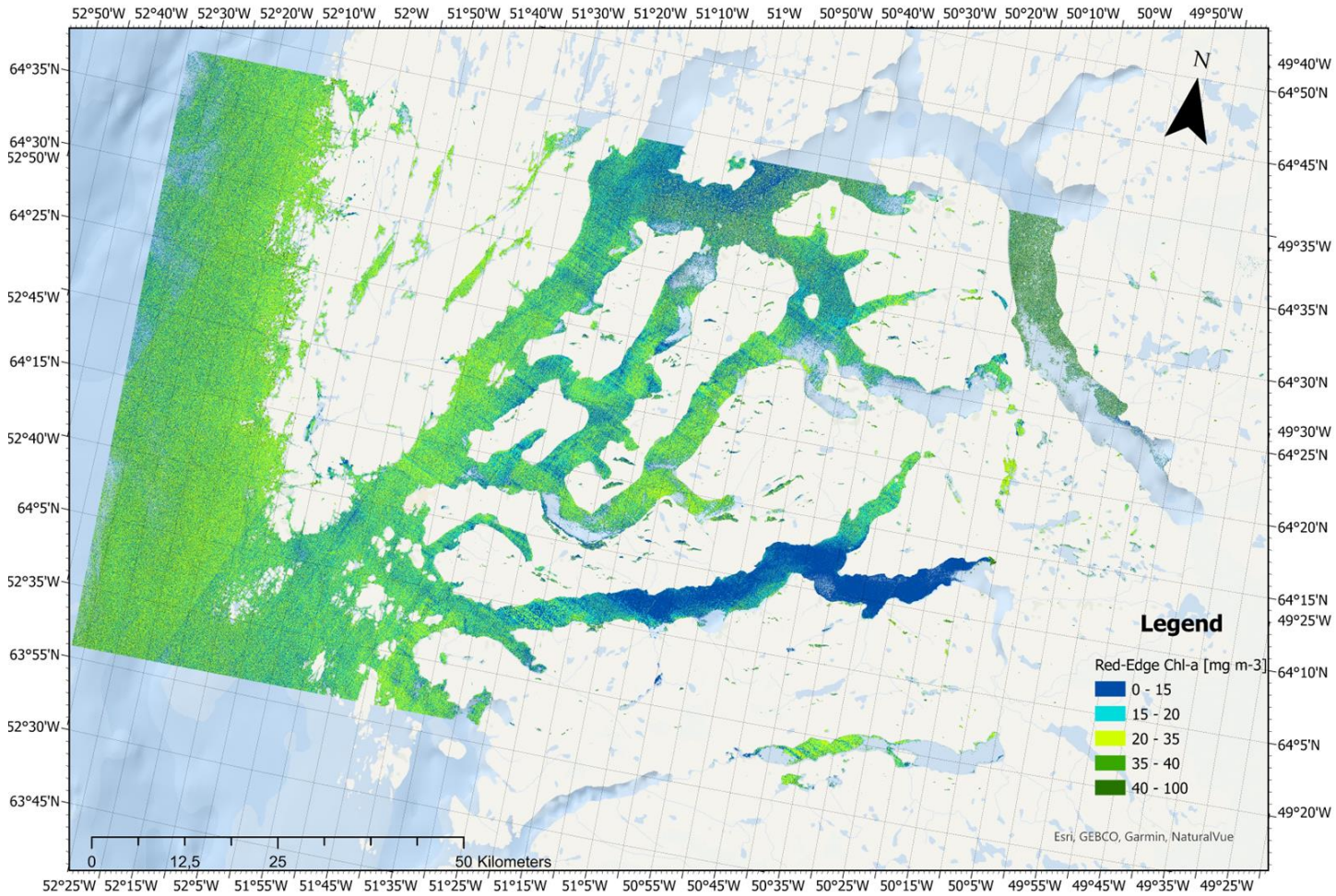

Figure 4. Chl-a estimates in [mg m-3] from the red-edge algorithm (Gons 2004) using S2A L1C scenes from the 22nd of June 2021.

The red-edge algorithm does not present well distinguishable areas in Chl-*a* concentrations, except for the Southern inlet of Nuup Kangerlua which has lower estimates than in the rest of the fjord (Figure 4). Chl-*a* estimates are generally much higher than in Figure 1 and 2. A noticeable number of pixels are missing data, in the Northern part of the fjord or offshore.

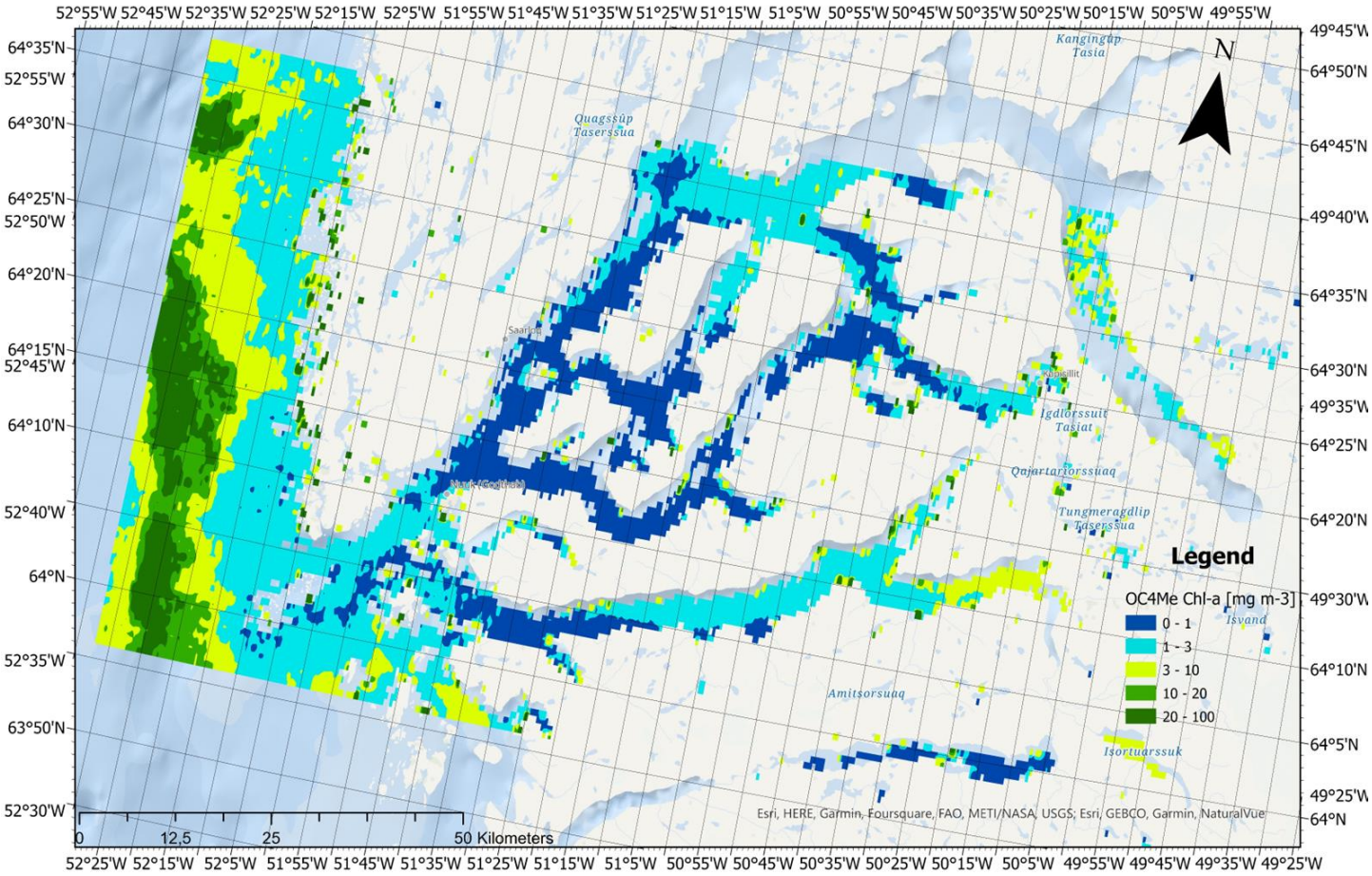

Figure 5. Chl-a estimates in [mg m-3] from the OC4Me algorithm (Morel et al. 2007) using S3A scenes from the 22nd of June 2021.

The OC4Me algorithm gives low Chl-a estimates in the middle of the fjord, while a clear hotspot is visible offshore (Figure 5). A considerable portion of the fjord, near the shores or in the middle part of some inlets, are missing data. The part of inlets near glaciers in the Eastern part present higher Chl-*a* estimates than in the rest of the fjord.

Table 2. Average and standard deviation of all pixels from the four different algorithms for the 22nd of June 2021.

Algorithm	Mean	Std. Dev.
OC3 (Pahlevan et al. 2020)	1.33	1.15
OC3L (derived from Cota 2004)	2.11	2.81
Red-edge (Gons 2004)	20.32	11.85
OC4Me (Morel et al. 2007)	5.26	9.79

The OC3 algorithm gives the lower Chl-*a* estimates on average. The distribution of the estimates is not spread out as indicates the low standard deviation (Table 2). The OC3L algorithm

presents higher values on average, with a wider distribution. The two algorithms have mean values of the same scale. The red-edge algorithm in the other hand, has values on average ten times higher and has a high standard deviation. Finally, the OC4Me algorithm gives Chl-*a* estimates noticeably higher than the two other blue-green ratio algorithms and has a higher standard deviation (Table 2). The scale is the same for the 9th and the 29th of July 2021 (cf. Appendixes 4 and 5).

3.2 Water properties

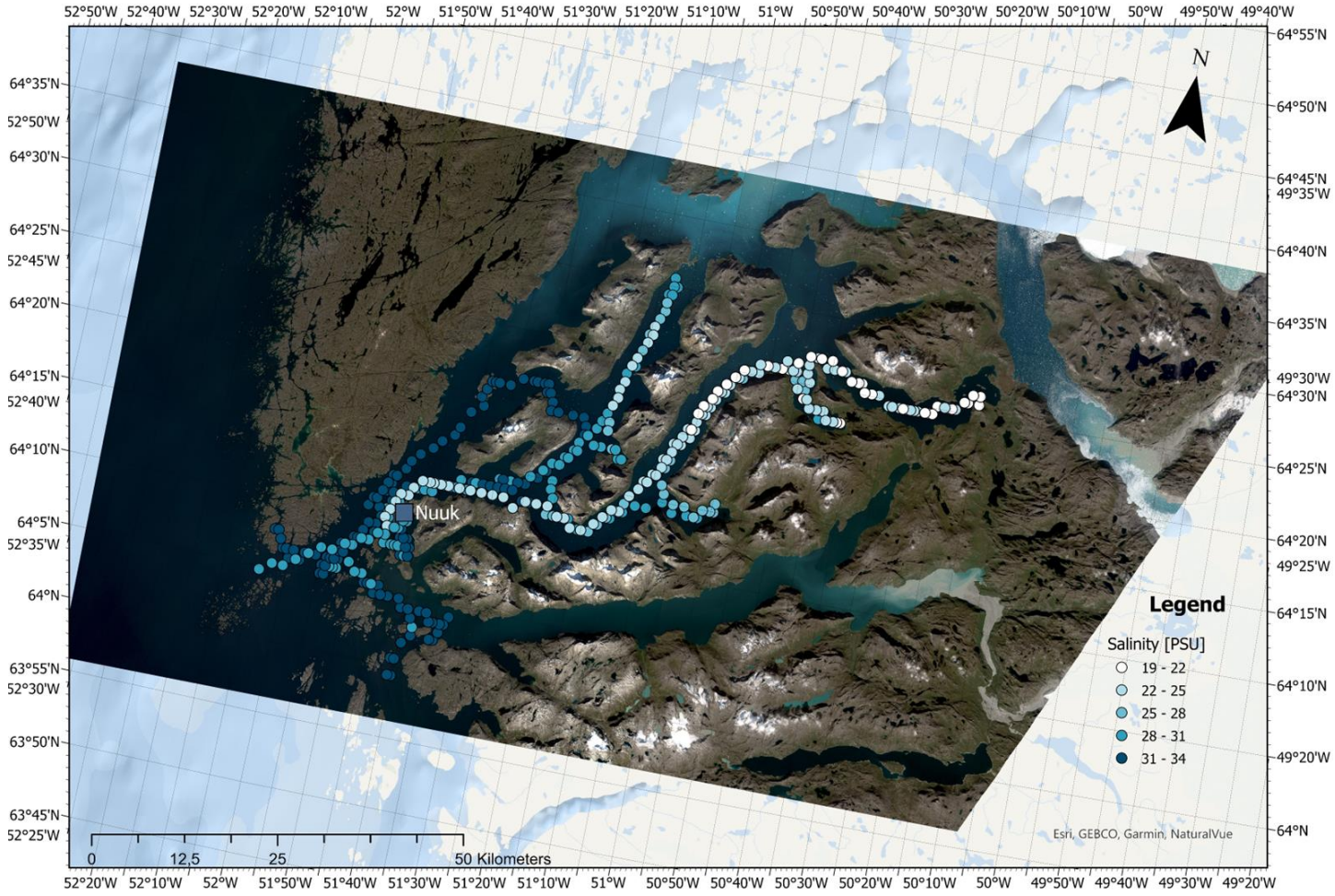

Figure 6. Salinity [PSU] from the CTD. Image from the 31st of August 2021.

The further East the ship went, the deeper it was in the fjord. It appears that the closer the ship was to glaciers, the lower was the salinity (Figure 6). Baffin Bay waters are saltier but still below the world ocean's average of 35 [PSU]. The salinity fluctuates in time as some area have high and low values. The ship made several travels inside the Nuup Kangerlua from Nuuk over a period of a month and a half.

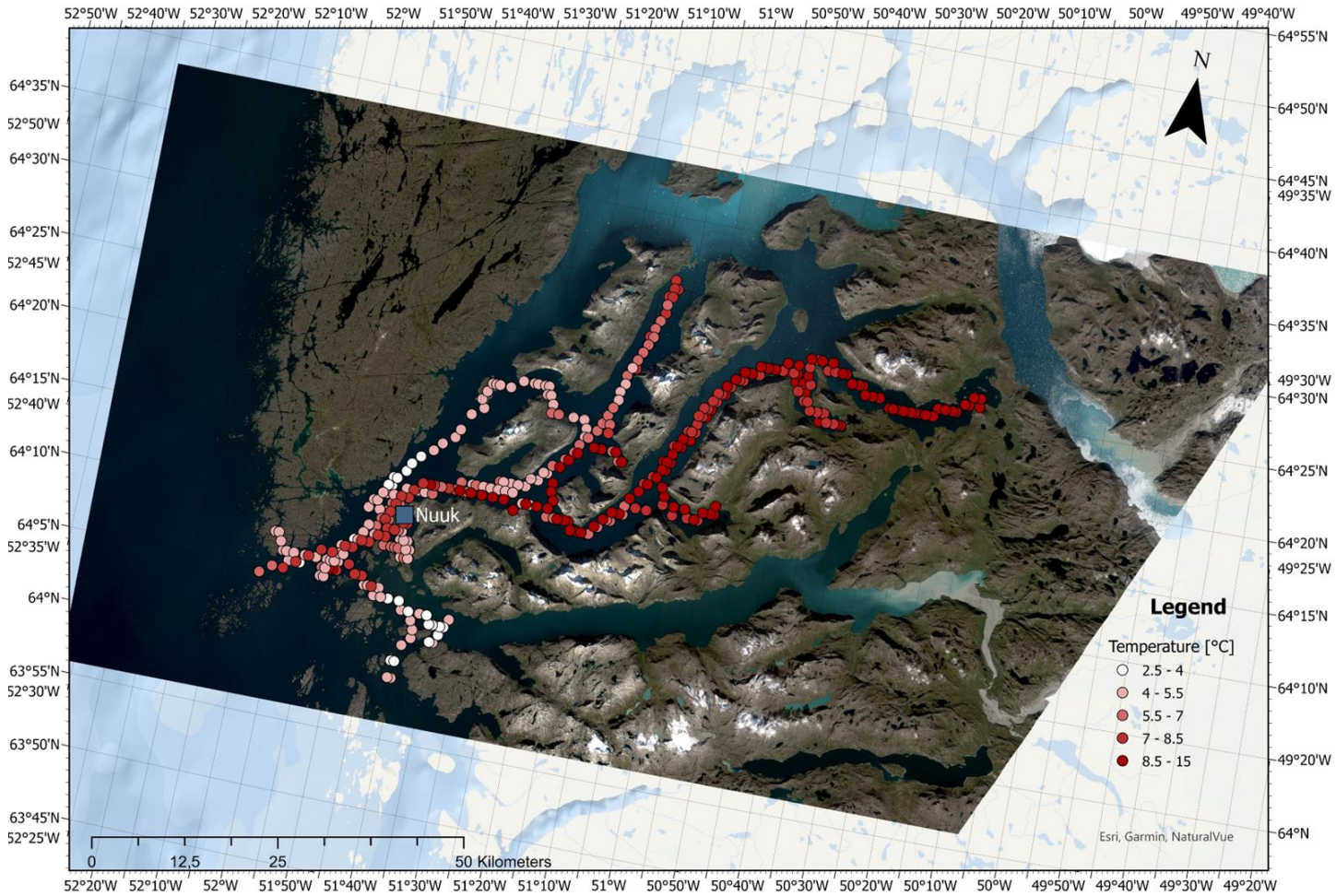

Figure 7. Surface water temperature [°C] from the CTD. Image from the 31st of August 2021.

The waters deep in the fjord present warmer temperatures than Baffin Bay waters (Figure 7). As for salinity, the temperature in one area can vary with time as some places present different values measured at different times.

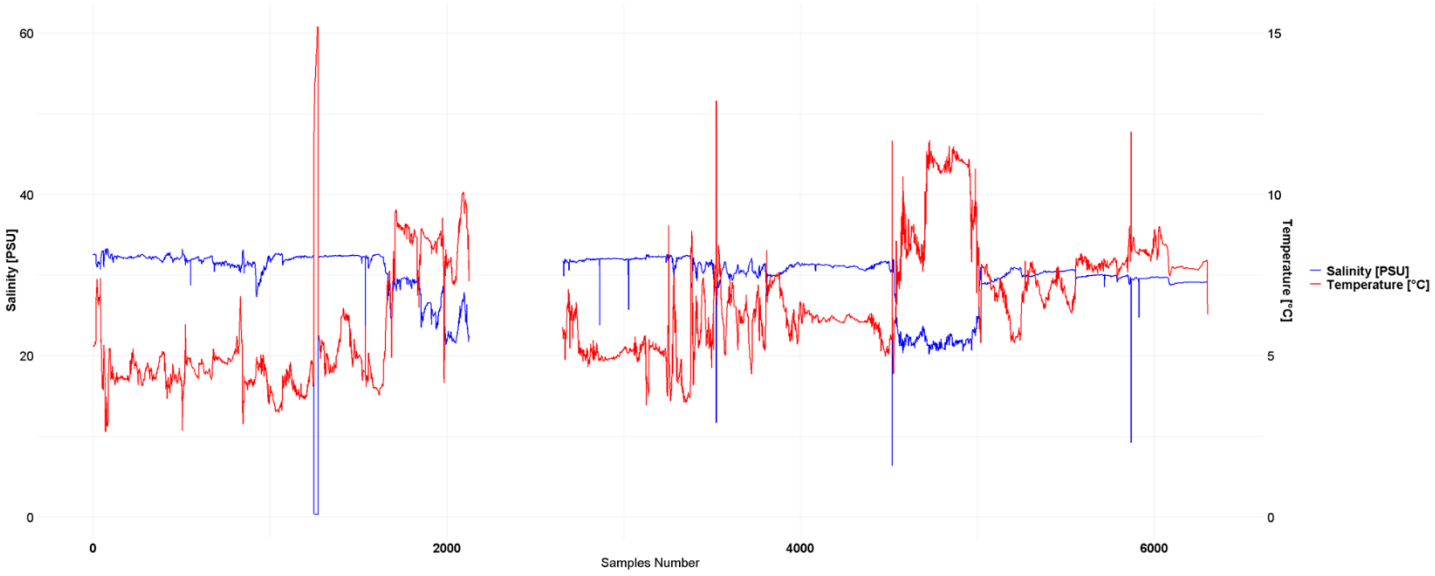

Figure 8. Salinity [PSU] and surface water temperature [°C] from the CTD, with a measure every 10 minutes between the 24th of June and the 6th of August 2021.

Salinity appears stable along the ship's route, with values generally above 30 [PSU] (Figure 8). Water temperatures present more variations, with limited spikes. Two distinct areas present lower salinity while having higher temperatures, before sample number 2000 and 5000. It corresponds to the incursions deep in Nuup Kangerlua, with more meltwater inputs. This visible delimitation between two water types coupled with the very stable salinity except for the two low spots mentioned above, led to separation of the data into two categories of water. The Nuup Kangerlua water with salinity below 28 [PSU] and Baffin Bay water with salinity above this threshold. The stability in salinity of Baffin Bay water is well repercussed in the low standard deviation presented in Table 3. This categorisation appears well suited as the standard deviations of each category, both for salinity and temperature, are lower than the total ones.

Table 3. Average and standard deviation of salinity [PSU] and surface water temperatures [°C] in regards of two different water types.

Water Type	Salinity [PSU]		Water Temperature [°C]	
	Mean	Std. Dev.	Mean	Std. Dev.
Nuup Kangerlua water	23.86	2.47	8.76	1.41
Baffin Bay water	31.26	0.94	5.62	1.28
Total	28.57	3.94	6.76	2.01

The vertical spikes in salinity and temperature are probably due to local contamination. The CTD did not collect data between the 8th and the 12th of July due to a technical issue, leading to the visible hole between samples number 2000 and 3000 (Figure 8).

3.3 Greenhouse gases

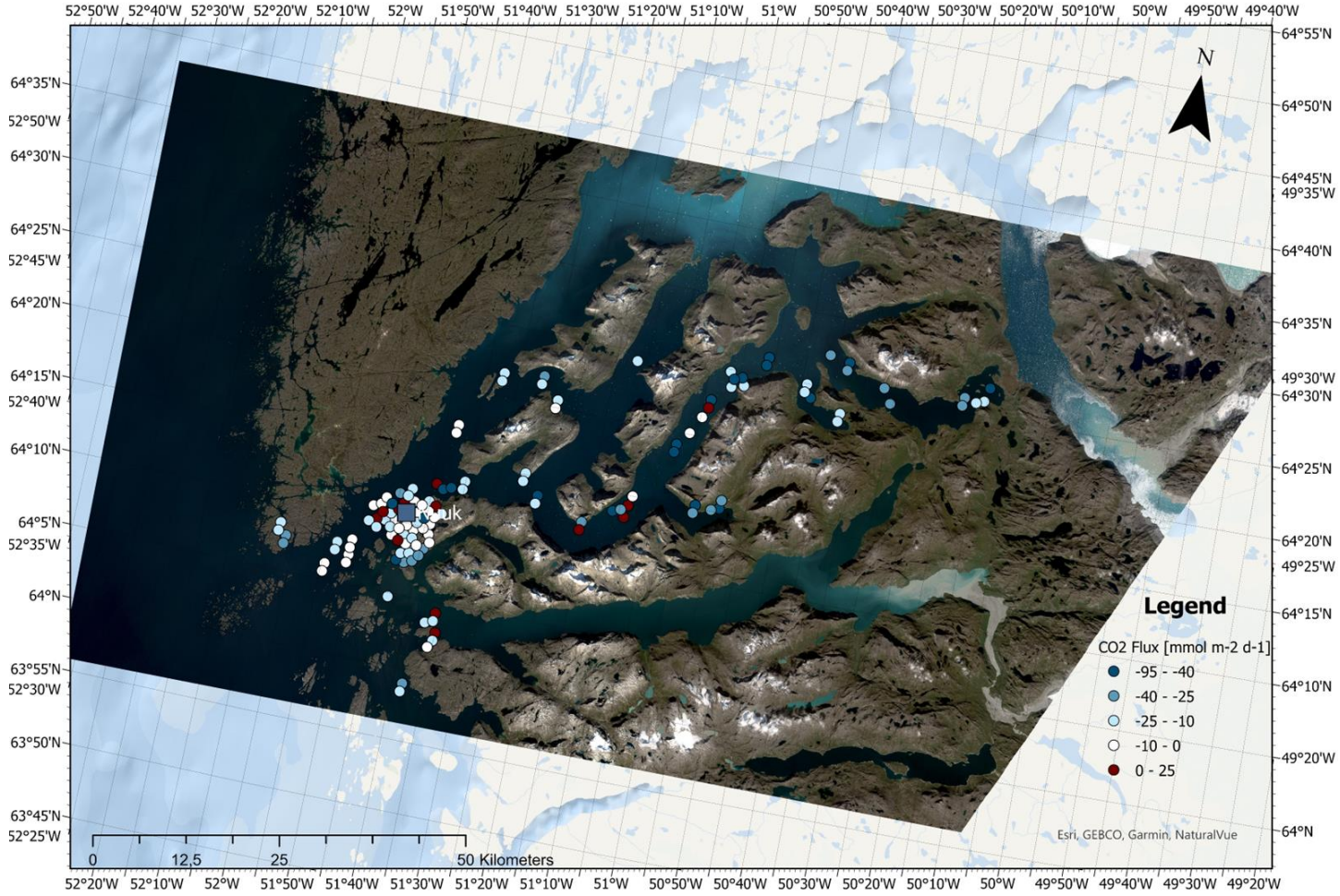

Figure 9. CO2 fluxes in [mmol m-2 d-1]. Image from the 31st of August 2021. Points have been dispersed to be more visible.

The majority of Nuup Kangerlua acts as a CO_2 sink (Figure 9). Only 13 samples out of the 132 present a positive flux. The waters deep in the fjord appears to be an important sink of CO_2 while waters close to the fjord's mouth are closer to equilibrium. The fluxes in Nuuk are more limited but are still generally negative.

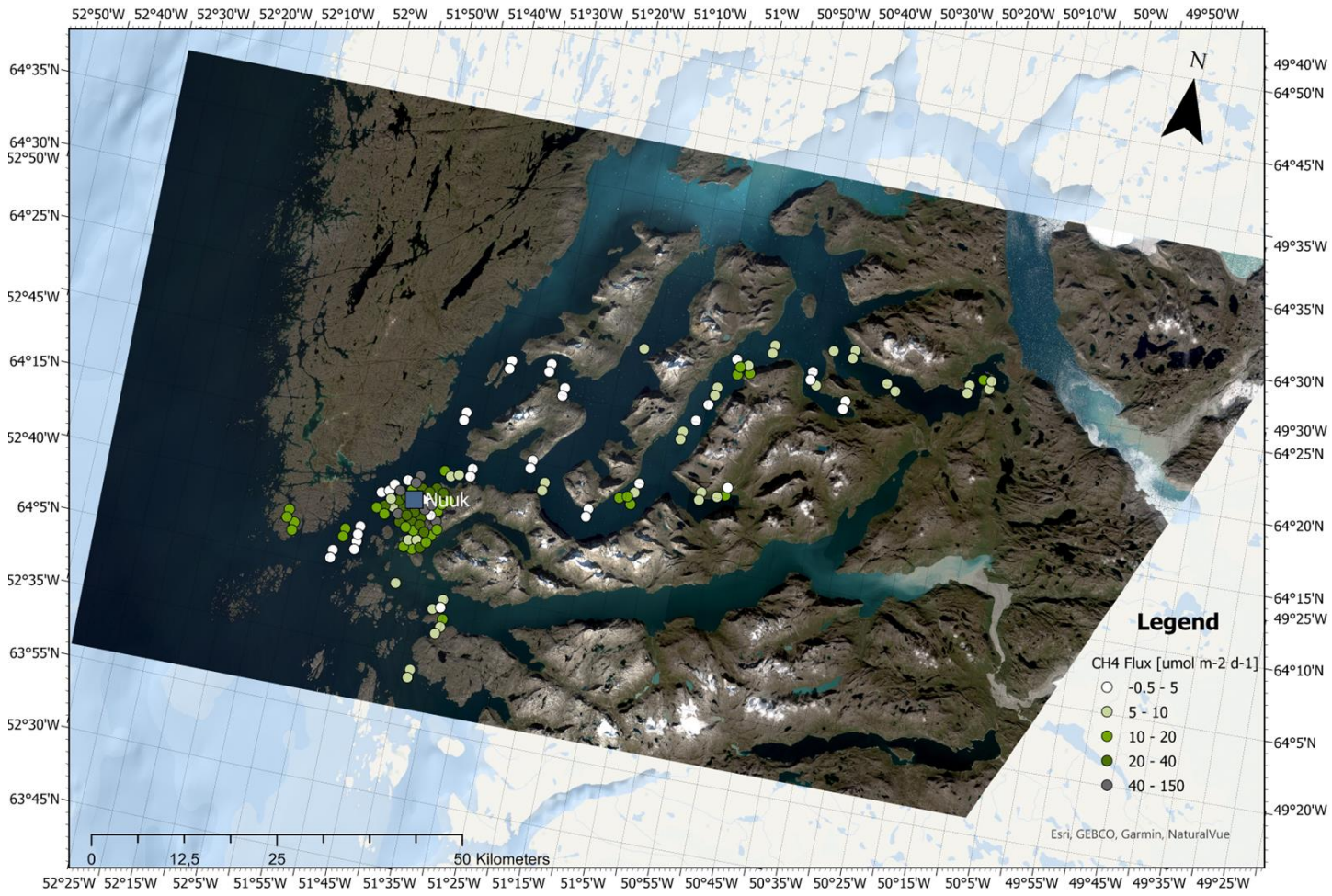

Figure 10. CH4 fluxes in [µmol m-2 d-1]. Image from the 31st of August 2021. Points have been dispersed to be more visible.

CH_4 fluxes are almost all positive across the dataset, meaning that Nuup Kangerlua is a source of CH_4 (Figure 10). The fluxes north of Nuuk and deep in the fjord are more limited than in Nuuk. The influence of the harbour is visible in the high fluxes observed in the capital of Greenland. As highlighted in Table 4, Nuuk is a hotspot of CH_4 emissions and with 39 samples out of the 132 in total, it has a weight in the total average. It also contributes to lower the sink of CO_2.

Table 4. Average and standard deviation of CO2 and CH4 fluxes with only Nuuk data, without it, or the total.

	CO_2 sea-air fluxes [mmol m^{-2} d^{-1}]		**CH_4 sea-air fluxes [µmol m^{-2} d^{-1}]**	
	Mean	**Std. Dev.**	**Mean**	**Std. Dev.**
Nuuk	-9.52	18.39	31.02	29.6
Without Nuuk	-21.05	15.89	7.81	5.65
Total	-17.65	17.42	14.67	19.74

4. Discussion

4.1 Comparison of the three algorithms used with S2A

Looking at Figures 1, 2, and 3, one of the algorithms stands out as being inappropriate for Chl-*a* estimates in Nuup Kangerlua. Indeed, the red-edge algorithm has been developed for productive waters with Chl-*a* concentrations between 3 and 185 [mg m^{-3}] (Gons 2002). It is at high concentrations that the peak of reflectance occurs at 705 [ηm] (Cota et al. 2003; Gons 2004). However, in the transect made by Meire et al. (2015) in Nuup Kangerlua, their *in situ* Chl-*a* estimates range between 0 and 14 [mg m^{-3}] in the first 40 meters of the water layer, with surface Chl-*a* being lower than the average. Even if Table 2 considers all the pixels in Figures 1 to 3, the high average value for the red-edge algorithm is out of range.

Figure 3 is very noisy, with high Chl-*a* estimates mixed with low estimates, reinforcing the unsuitability of this algorithm. In addition, the red-edge algorithm is not correlated in all three dates with the OC3L algorithm which is in range (cf. Table 2) with Meire et al. (2015) data (cf. Appendixes 6, 7, and 8).

Both OC3 and OC3L algorithms are in range with Meire et al. (2015) *in situ* data (cf. Table 2 and Appendixes 4 and 5). They are also well correlated (cf. Appendixes 9, 10, and 11), which is why only one of them was compared with the red-edge algorithm. This is not surprising as they rely on the exact same wavelengths, used in the same ratio (cf. Chapter 2.3).

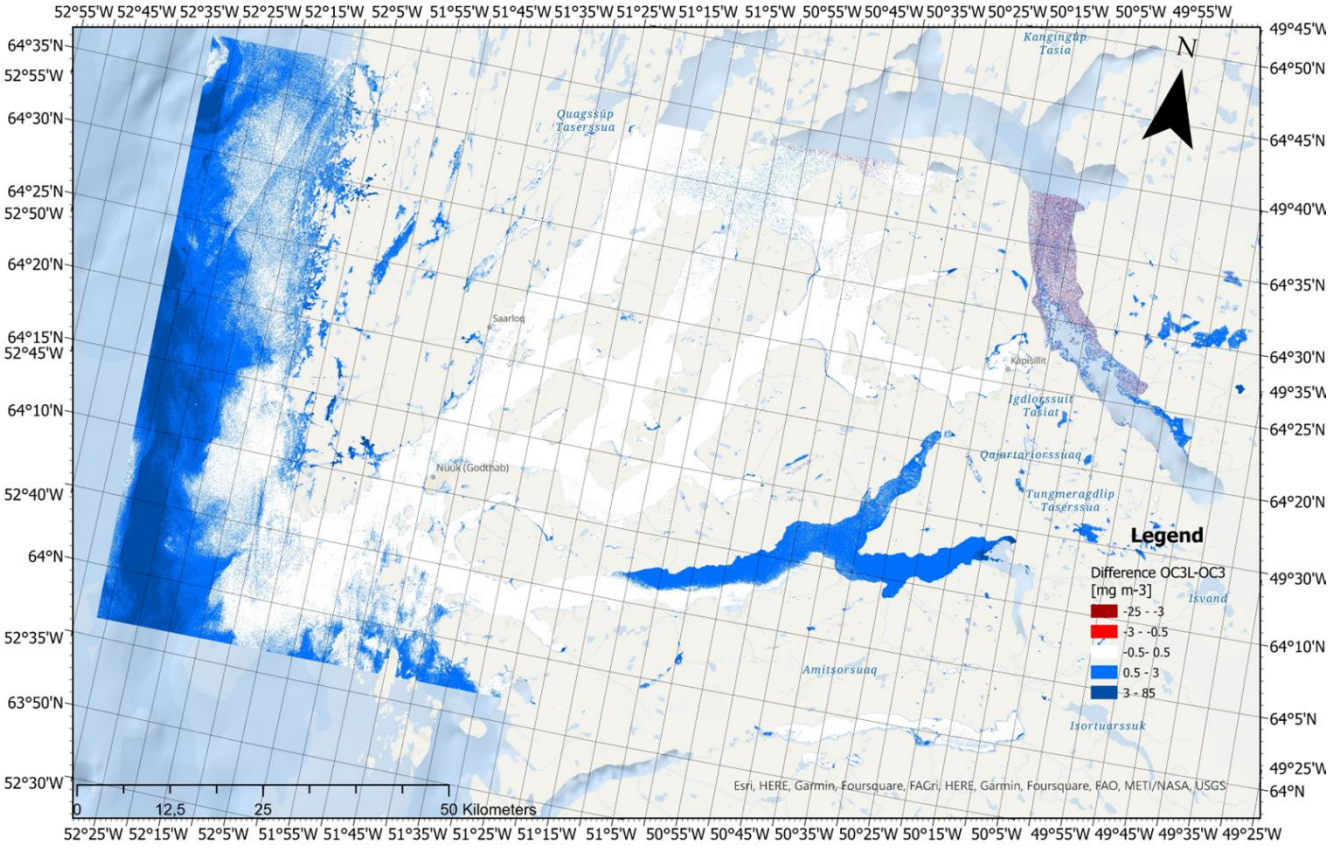

Figure 11. Difference OC3L – OC3 in [mg m-3] for the 22nd of June 2021. Positive values are when OC3L > OC3.

The OC3L presents no real changes (white pixels) or higher estimates than the OC3 algorithm, for almost all pixels in the fjord (Figure 11). The scale is still similar (cf. Table 2 and Appendixes 4 and 5), and the higher estimates trend stands true for all three dates. It is coherent with the aim of this algorithm as the OC4L algorithm (which is the basis of the derived OC3L) is increasing the Chl-*a* estimates for values over 0.6 [mg m^{-3}] and reducing the estimates below this threshold in comparison with the OC4V4 algorithm (Cota 2004; O'Reilly et al. 2000). The OC3L does the same in comparison with the OC3 as this algorithm is not tuned for arctic waters just like the OC4V4. The signal is not clear in the Northern inlet, probably due to the presence of sea-ice and icebergs. Most of the pixels inside Nuup Kangerlua present no changes between the two algorithms for all three dates (cf. Figure 11 and Appendixes 12 and 13).

Even though the OC3L is only derived from another algorithm without calibration, it still presents coherent estimates in regard to the OC3 algorithm. It gives slightly higher estimates, which is expected, and these appear more in line with the *in situ* data of Meire et al. (2015) and the OC4Me estimates. It was thus selected to be tested with the GHGs fluxes and dissolved concentrations.

4.2 Comparison with OC4Me from S3A

The OC4Me algorithm provides higher estimates on average for each of the three dates (cf. Table 2 and Appendixes 4 and 5). Looking at Figures 2, 3, and 5, this algorithm appears to give estimates in line with the OC3 and OC3L algorithms for the 22nd of June 2021. It reinforces the overall validity of the estimates made with S2A, as another instrument (OLCI on S3A) and another algorithm (similar but using 4 bands instead of 3) get to the overall same conclusions.

S3A Ocean products have already been processed for atmospheric corrections[6] and show good results (Binh et al. 2022; Zhou et al. 2023) even though it might underestimate Chl-*a* for very low values (>0.1 [mg m^{-3}]) (Tilstone et al. 2021). In addition, the volume of data is lower, facilitating their use and processing time. Even though the exact revisit time of S3A is longer than S2A, the much wider scenes allow to have images of the same place more frequently which is important to follow closely the evolution of Chl-*a* concentrations and to not miss blooms.

However, S3A scenes have a lower spatial resolution in comparison with S2A. The 300x300 m^2 pixels are enough to treat open sea or very large water bodies but the complexity of the ramifications of a fjord is too high for this precision. In Figure 4, a lot of pixels are missing data in the fjord, sometimes cutting the inlets in half. The pixels near the shores are also probably influenced by the reflectance of land. By extracting the values under the 132 samples points from the GHGs dataset, only 51 have a OC4Me value. The OC4Me algorithm is thus not well suited for the Nuup Kangerlua and this study. Still, it is interesting to reinforce the validity of the S2A estimates and to compare them in more depth.

[6] Sentinel online, https://sentinel.esa.int/web/sentinel/technical-guides/sentinel-3-olci/level-2/ocean-processing

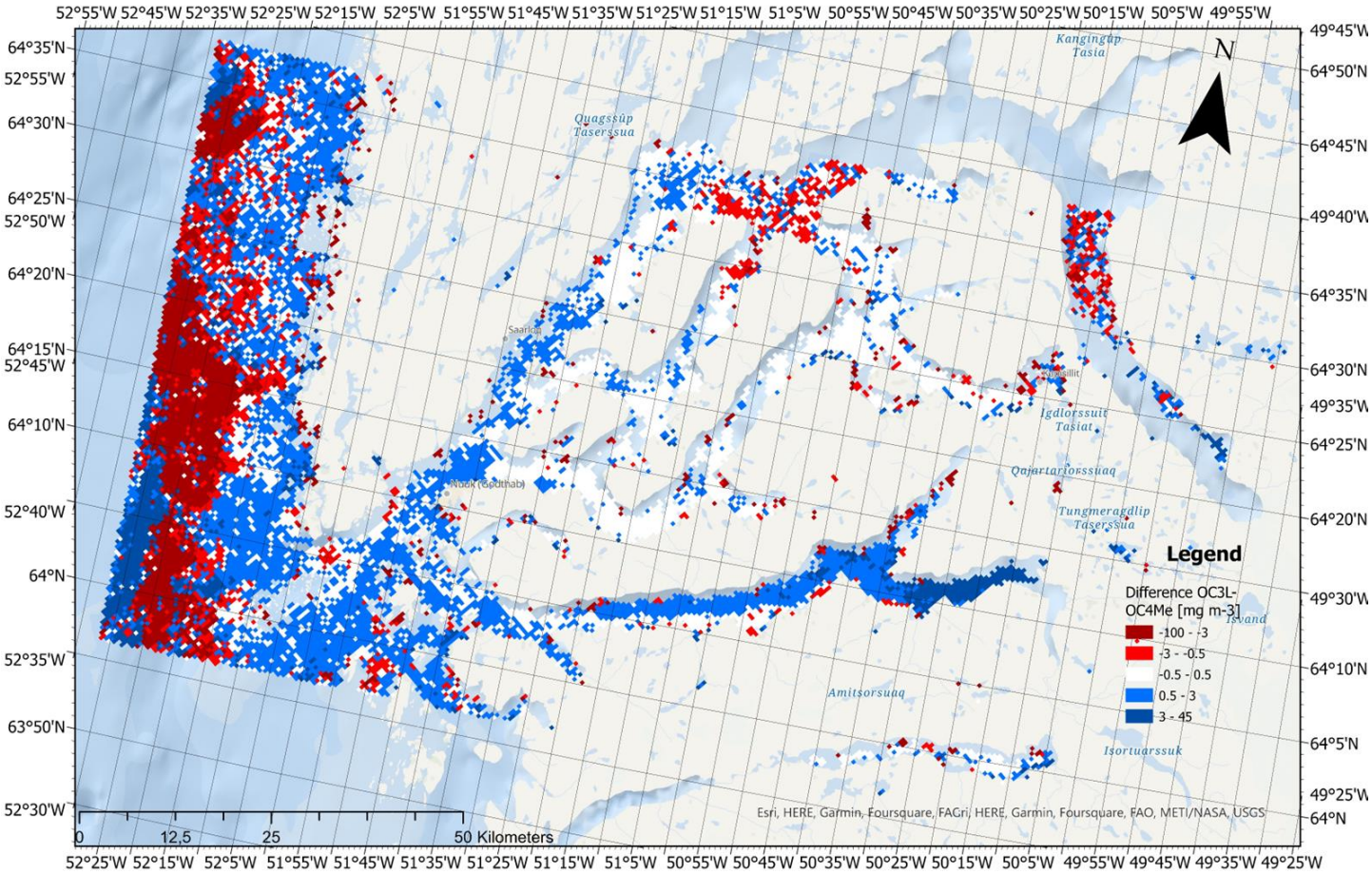

Figure 12. Difference OC3L – OC4Me in [mg m-3] for the 22nd of June 2021. Positive values are when OC3L > OC4Me. Max value for OC3L pixels.

The OC3L and OC4Me algorithms are not as close as the OC3L and the OC3, but they still give similar estimates as most of the pixels vary of 3 [mg m^{-3}] or less (Figure 12). Due to the difference in spatial resolution, the maximum value of the OC3L algorithm was chosen to be compared with the corresponding value of the bigger pixel from OC4Me. The region with the lesser variations is inside Nuup Kangerlua whereas the open sea in the West presents high positive and negative variations adjacent to one another. The OC3L has more pixels higher than the OC4Me, but the average value is lower, meaning that the hotspot identified offshore is very high with OC4Me estimates. Appendixes 14 and 15 shows that the OC4Me and OC3L estimates are close for all three dates, even if, for the 8-9th of July and the 28-29th of July, the OC4Me generally gives higher results.

The Southern inlet (in blue in Figure 12 and for some parts in Appendixes 14 and 15) appears to be a consistent place where the OC3L algorithm gives higher estimates than the OC4Me, especially at its source, near the glacier. This could indicate that the OC3L is more subject to overestimation in the presence of CDOM than the OC4Me and be caused by the missing band 510 [ηm].

4.3 Chlorophyll-a estimates and greenhouse gases fluxes

The OC3, OC3L and OC4Me estimates all indicate that surface waters inside the Nuup Kangerlua are not highly productive waters and present low Chl-*a* estimates. It is coherent with the results of Meire et al. (2015), even if they found a subsurface Chl-*a* spring bloom, because the period covered in this work does not include spring. Although the remote sensing Chl-*a* estimates present uncertainties (Pahlevan et al. 2021) due to atmospheric corrections and algorithms and that these uncertainties are enhanced by the lack of calibration with *in situ* data in this study, it is still relevant to test if there is a visible link between the OC3L estimates and GHGs fluxes. To find a relationship between Chl-*a* and GHGs fluxes would reinforce the validity of the estimates as there should be a link. Indeed, higher Chl-*a*, meaning higher NPP, leads to a diminution of dissolved CO_2 concentrations through photosynthesis, a phenomenon visible in Nuup Kangerlua mostly during spring, according to Meire et al. (2015). Higher Chl-*a* also leads to higher dissolved CH_4 concentrations through the decomposition of organic matter by methanogenic *Archaea* in anaerobic environments (Saunois et al. 2020).

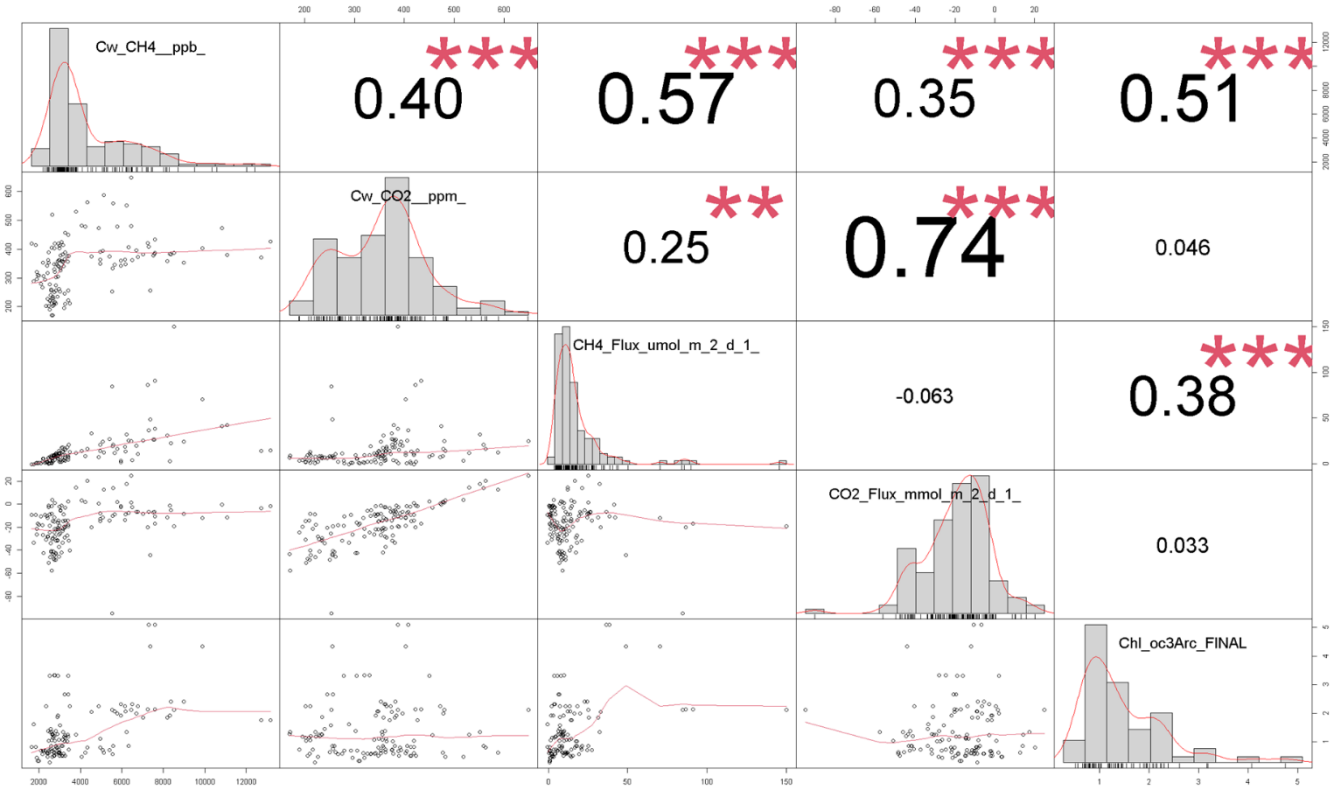

Figure 13. Matrix of correlation between dissolved CH4 and CO2 and their sea-air fluxes, with the OC3L (Chl_oc3Arc_FINAL) estimates at sampling points. Cw stands for "dissolved concentrations".

Figure 13 shows a correlation between Chl-*a* estimates and CH_4, particularly with dissolved concentrations as fluxes are influenced by additional external factors, such as wind speed (McGinnis et al. 2015). As for CO_2, no signal appears indicating that other factors influenced dissolved CO_2 and fluxes during the period of measurements. These results are confirmed by Appendix 16. The lack of correlation between CO_2 and Chl-*a* is not a problem as Rysgaard et al. (2012) also found no correlation between annual NPP and CO_2 uptake in Nuup Kangerlua, underlining the fact that CO_2 fluxes are controlled by other factors.

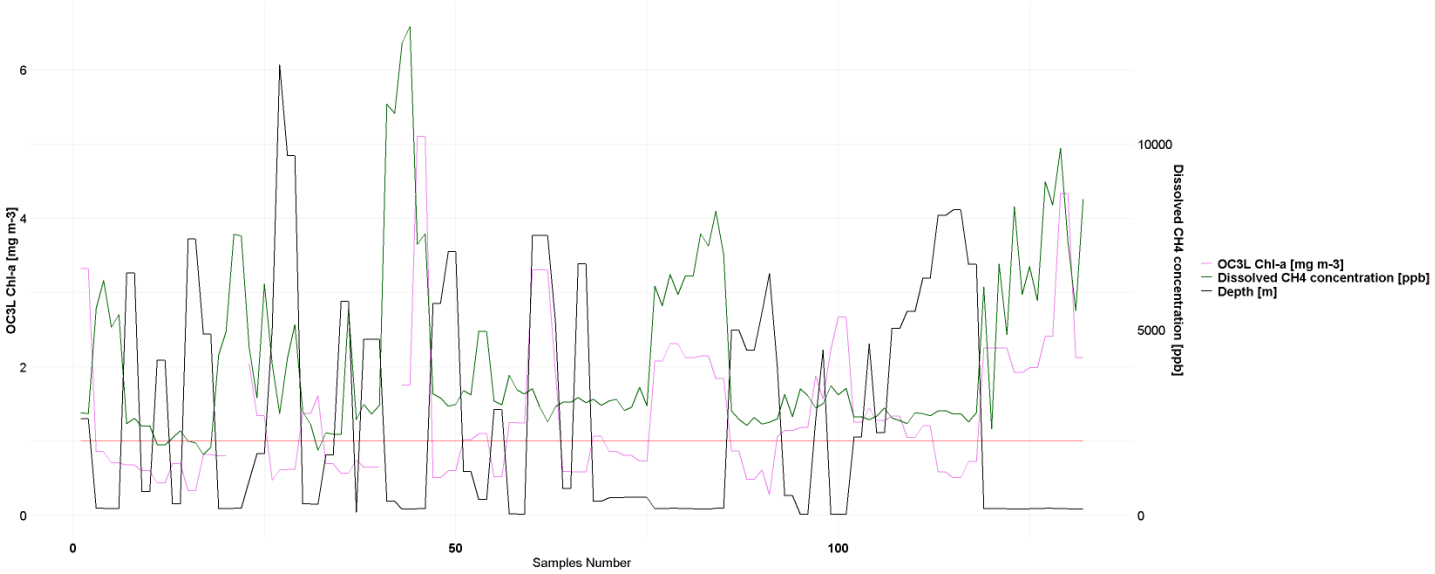

Figure 14. OC3L estimates at sampling points (pink), dissolved CH4 concentrations (green) and depth (black). The red horizontal line indicates a depth of 100 [m] and is the reference for the depth line in black.

Figure 14 further emphasizes the link between Chl-*a* estimates and dissolved CH_4 concentrations, with most of the spikes in Chl-*a* happening simultaneously as spikes in CH_4 concentrations. Some Chl-*a* hotspots do not seem to influence CH_4, for example in the first samples or around sample 60. These uncorrelated spikes of Chl-*a* happened over deep waters, suggesting that depth is a factor influencing both CH_4 and the link between CH_4 and Chl-*a*. Indeed, it is a recognized factor impacting dissolved CH_4 and fluxes. Sediments are producing CH_4 because they contain anoxic environments (Arctic Monitoring and Assessment Programme (AMAP) 2015; Saunois et al. 2020). They will have an impact on surface waters when depth is shallow, with a threshold of 100 [m] (McGinnis et al. 2006). Shallower waters present higher CH_4 fluxes than deep waters (Weber et al. 2019). It is also what Table 5 indicates. The bias of Nuuk identified in Chapter 3.3 has an influence on this result as Nuuk is a harbour and thus present shallow waters, high CH_4 fluxes and high Chl-*a* concentrations potentially due to human activities. It drives the mean of shallow waters up, and combined with the high standard deviation of this category, it means that shallow waters do not necessarily lead to high dissolved CH_4 concentrations and completely limit the conclusions that can be drown from Figure 14 and 15.

Table 5. Average and standard deviation of CO2 and CH4 fluxes with two depth categories.

Depth	**Dissolved CH_4 concentrations [ppb]**		**CH_4 sea-air fluxes [µmol m^{-2} d^{-1}]**	
	Mean	**Std. Dev.**	**Mean**	**Std. Dev.**
<100 [m]	5189	2611	20.6	24.33
Deep	2810	665	6.85	4.45
Total	4162	2332	14.67	19.74

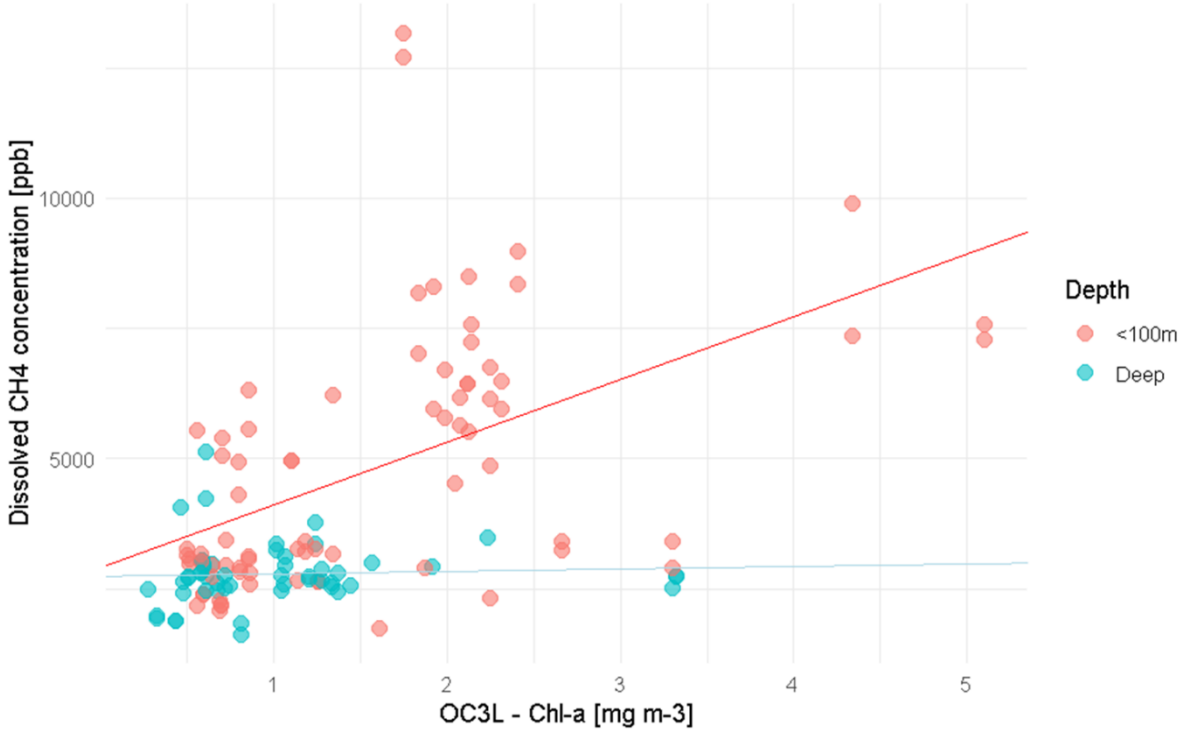

Figure 15. Scatter plot of OC3L estimates and dissolved CH4. The red line is the linear regression line for points with a depth shallower than 100 [m]. The blue line is the linear regression line for points with a depth superior as 100 [m].

Figure 15 underlines the interaction between Chl-*a* and depth to explain dissolved CH_4 concentrations. Depth or Chl-*a* alone explain less dissolved CH_4 than when these two factors interact. It explains why some spikes of Chl-*a* or some shallow waters are not necessarily linked with high dissolved CH_4 concentrations. However, due to the presence of Nuuk's samples, which can be considered as an intermediate variable in this relationship, it would be bold to affirm that Chl-*a* and depth are drivers of the CH_4 fluxes.

4.4 The Nuup Kangerlua's hydrology and greenhouse gases fluxes

Due to meltwater inputs and a complex topography, fjords have a specific hydrology which has an impact on GHGs fluxes. Figure 8 and Table 3 allowed to identify two main water types, the water from the fjord with meltwater origins and the water from Baffin Bay entering the fjord from offshore.

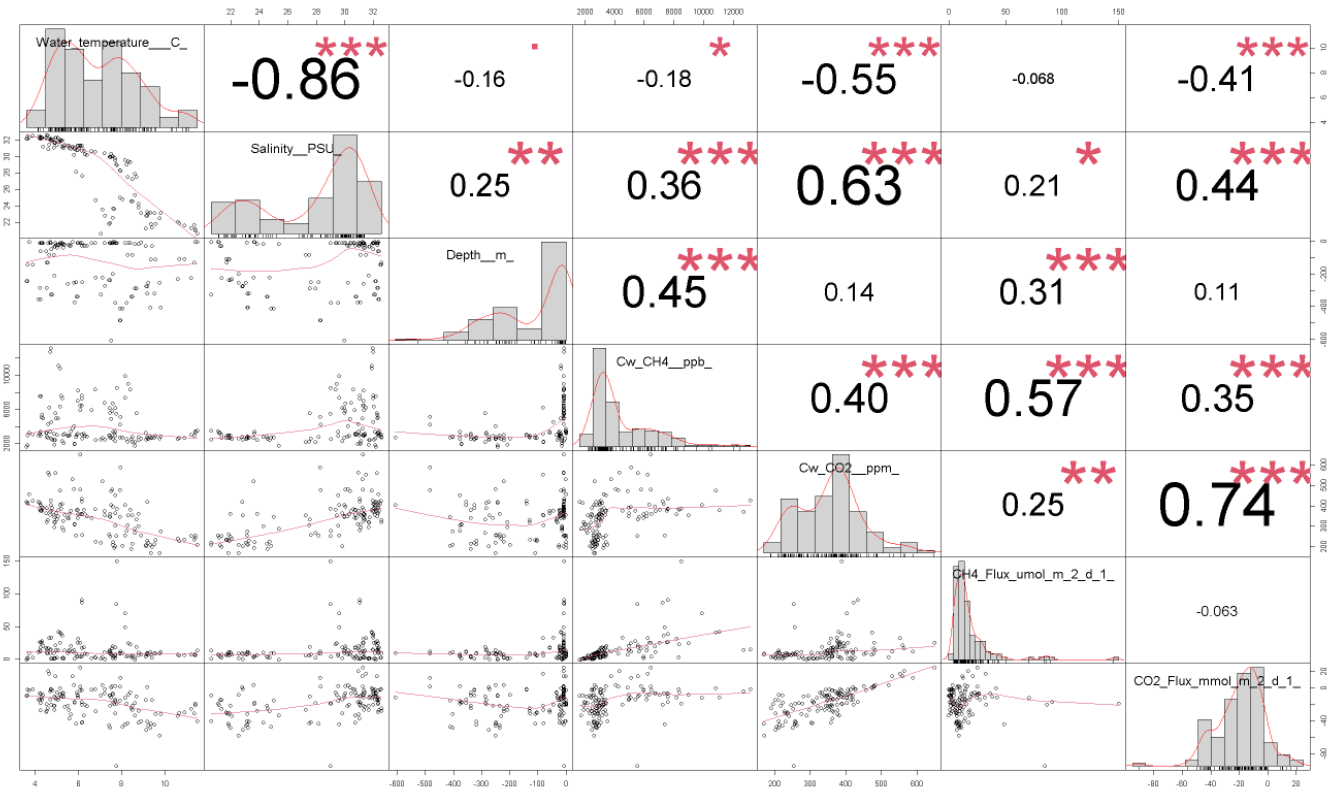

Figure 16. Matrix of correlation between dissolved CH4 and CO2 and their sea-air fluxes, with water temperature [°C], salinity [PSU] and depth [m]. Cw stands for "dissolved concentrations".

Figure 16 underlines the very strong relationship between salinity and temperature, creating two distinct water types. These are also correlated with GHGs, particularly dissolved CO_2 concentrations.

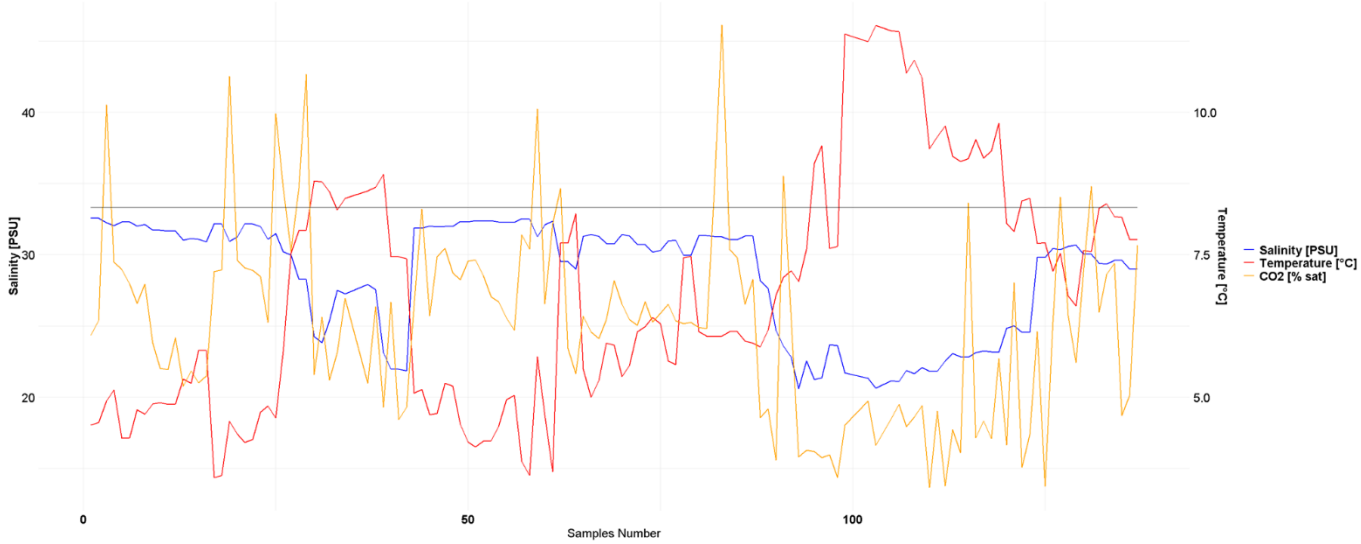

Figure 17. Salinity [PSU] (blue), water temperature [°C] (red) and percentage of saturation of dissolved CO2 (orange).

Percentage of saturation is a good variable to observe at the same time the dissolved concentrations and the localisation of positive fluxes, when saturation exceeds 100 [%]. In Figure 17, it is visible that CO_2 saturation decreases when salinity decreases, meaning that the Nuup Kangerlua waters are a strong sink of CO_2. This is due to meltwater inputs, which present a low CO_2 saturation. This result is in line with the study of Meire et al. (2015) who identified glacial meltwater as a driver of negative CO_2 flux. Appendix 17 emphasizes the strong difference between the two water types identified with Figure 8 and Table 3 regarding CO_2.

Table 6. Overview of CO_2 sea-air fluxes around Greenland.

Studies	**CO_2 sea-air fluxes [mmol m^{-2} d^{-1}]**	**Regions**
This study	-17.65 (±17.42)	Nuup Kangerlua
(Meire et al. 2015)	-14.84	Nuup Kangerlua
(Rysgaard et al. 2012)	-18.95 to -24.66	Gothabsfjord entrance
(Meire et al. 2015)	-12.5 to -50	Fyllas Banke Shelf (offshore of Nuup Kangerlua)
(Chen et al. 2013 in Meire et al. (2015))	-3.33	Fyllas Banke Shelf (offshore of Nuup Kangerlua
(Sejr et al. 2011)	-7.31	Young Sound (Eastern Greenland)
(Nakaoka et al. 2006)	-11.87	Greenland Sea (Eastern Greenland)

The CO_2 fluxes found in this study are in line with the rest of the literature (Table 6). The results from the Fyllas Banke shelf do not contradict the lower uptake from Baffin Bay waters in comparison with Nuup Kangerlua waters from this work. The value from Rysgaard et al. (2012) come from a multi annual dataset and is a yearly mean converted into a daily mean. These authors found an even greater sink of CO_2 during some months and emissions of CO_2 during

three periods out of their 6 years of measurements. They emphasize the high inter annual variability, limiting the use of short term, one and a half month-long, study.

Table 7. Average and standard deviation of CH4 dissolved concentrations and fluxes with the two water types identified with Figure 7 and Table 3.

Water Type	**Dissolved CH_4 concentrations [ppb]**		**CH_4 sea-air fluxes [µmol m^{-2} d^{-1}]**	
	Mean	**Std. Dev.**	**Mean**	**Std. Dev.**
Nuup Kangerlua water	3040	1106	11.64	23.58
Baffin Bay water	4802	2598	16.4	17.08
Total	4162	2332	14.67	19.74

For CH_4, a strong relationship with water types such as for CO_2 is not visible. Still, Nuup Kangerlua waters appear to be less saturated in CH_4 than Baffin Bay waters. The higher average fluxes in Baffin Bay water are driven by the presence of Nuuk which was filled with this type of water during the majority of the measurement period. It does not mean that fjords are low emitters of CH_4. Indeed, Bonaglia et al. (2022) identified fjords as strong emitters of CH_4. In comparison with the rest of the literature, the results of this study are in the lower end for CH_4 fluxes in arctic fjords (cf. Appendix 18). The meltwater inputs create a very stratified water column and sills at the entrance of fjords reduce even more the mixing of deep water laying at the bottom of fjords (Straneo et Cenedese 2015). It results in deep waters depleted of oxygen. The high CH_4 source is thus located at seabed and is emitted in the atmosphere during mixing event (Bonaglia et al. 2022), not necessarily captured in this study.

5. Limitations

There are several limitations to this work, both regarding Chl-*a* estimates and the GHGs dataset. As mentioned before, remote sensing of Chl-*a* is challenging, especially in the Arctic (cf. Chapter 1.1.1). All the steps leading to Chl-*a* estimates, from the capture of surface reflectance by satellites to atmospheric corrections and Chl-*a* algorithms, are subject to uncertainties. In the absence of calibration with *in situ* data, all the strict numbers of Chl-*a* advanced in [mg m^{-3}] are not to be taken as exact values but only aim at providing the tendencies visible from space.

The GHGs dataset suffers from covering a too short period of time in order to understand all the processes influencing GHGs fluxes over a year. In addition, most of the samples do not come from the same sampling sites, except for Nuuk, which removes the possibility of creating a proper time series. On the other hand, the important number of samples coming from Nuuk is a bias in the results as it is a harbour influenced by human activities.

With the ongoing global warming, processes are evolving and complexifying the comparison with previous studies.

Finally, the GHGs dataset has been partially collected manually on a sailing ship, implying field hazards, mistakes, or contamination. All samples were studied to find those with potential mistakes which were removed. This process is described in Appendix 3. It is possible that mistakes were overseen or that some samples were wrongfully removed.

6. Conclusion

Both the OC3 and OC3L algorithms used with S2A scenes give results coherent with the literature and with a spatial resolution sufficiently high to retrieve Chl-*a* estimates in Nuup Kangerlua. In order to improve the precision of estimates, a calibration with *in situ* data would be welcome. The OC4Me algorithm used with S3A scenes is great to have quick and ready-to-use estimates of Chl-*a* and can provide more continuous data as images are produced more frequently for the same places but the spatial resolution is still too low to cover a complex area such as the Nuup Kangerlua.

As for GHGs, the Nuup Kangerlua is an important sink of CO_2 with an average of -17.65 (±17.42) [mmol m^{-2} d^{-1}]. It corresponds to an annual uptake of approximatively -77 [g C m^{-2} y^{-1}]. It is an emitter of CH_4 with an average of 14.67 (±19.47) [µmol m^{-2} d^{-1}] during the period of measurements. It corresponds to annual emissions of approximatively 0.06 [g C m^{-2} y^{-1}]. Glacial meltwater inputs are a driver of the strong CO_2 uptake while no main driver of the CH_4 fluxes was identified.

To be able to understand the precise GHGs fluxes in Nuup Kangerlua over a year and thus reduce the uncertainties surrounding this key step of the carbon cycle, a study based on periodic measurements at fixed places in the fjord during the year, with data including Chl-*a* for the calibration of algorithms, would be necessary. It would be well suited to compare and update the work from Rysgaard et al. (2012) and Meire et al. (2015). Such a robust dataset could be used to model the GHGs fluxes, in particular CH_4, with a high spatial resolution thus lowering the uncertainties surrounding the CH_4 cycle in fjords.

Bibliography

Arctic Monitoring and Assessment Programme (AMAP). 2015. *AMAP Assessment 2015: Methane as an Arctic climate forcer*. https://www.amap.no/documents/doc/AMAP-Assessment-2015-Methane-as-an-Arctic-forcer/1285.

Arrigo, Kevin R., et Gert L. van Dijken. 2011. « Secular Trends in Arctic Ocean Net Primary Production ». *Journal of Geophysical Research: Oceans* 116(C9). doi: 10.1029/2011JC007151.

Arrigo, Kevin R., Patricia A. Matrai, et Gert L. Van Dijken. 2011. « Primary Productivity in the Arctic Ocean: Impacts of Complex Optical Properties and Subsurface Chlorophyll Maxima on Large-scale Estimates ». *Journal of Geophysical Research: Oceans* 116(C11):2011JC007273. doi: 10.1029/2011JC007273.

Arrigo, Kevin R., et Gert L. Van Dijken. 2015. « Continued Increases in Arctic Ocean Primary Production ». *Progress in Oceanography* 136:60-70. doi: 10.1016/j.pocean.2015.05.002.

Binh, Nguyen An, Pham Viet Hoa, Giang Thi Phuong Thao, Ho Dinh Duan, et Phan Minh Thu. 2022. « Evaluation of Chlorophyll-a Estimation Using Sentinel 3 Based on Various Algorithms in Southern Coastal Vietnam ». *International Journal of Applied Earth Observation and Geoinformation* 112:102951. doi: 10.1016/j.jag.2022.102951.

Bonaglia, Stefano, Tobias Rütting, Mikhail Kononets, Anders Stigebrandt, Isaac R. Santos, et Per O. J. Hall. 2022. « High Methane Emissions from an Anoxic Fjord Driven by Mixing and Oxygenation ». *Limnology and Oceanography Letters* 7(5):392-400. doi: 10.1002/lol2.10259.

Carmack, Eddy, David Barber, Jens Christensen, Robie Macdonald, Bert Rudels, et Egil Sakshaug. 2006. « Climate Variability and Physical Forcing of the Food Webs and the Carbon Budget on Panarctic Shelves ». *Progress in Oceanography* 71(2-4):145-81. doi: 10.1016/j.pocean.2006.10.005.

Chen, Jiang, Weining Zhu, Yong Q. Tian, Qian Yu, Yuhan Zheng, et Litong Huang. 2017. « Remote Estimation of Colored Dissolved Organic Matter and Chlorophyll-a in Lake Huron Using Sentinel-2 Measurements ». *Journal of Applied Remote Sensing* 11(03):1. doi: 10.1117/1.JRS.11.036007.

Cota, G. 2004. « Transformation of Global Satellite Chlorophyll Retrievals with a Regionally Tuned Algorithm ». *Remote Sensing of Environment* 90(3):373-77. doi: 10.1016/j.rse.2004.01.005.

Cota, Glenn F., W. Glen Harrison, Trevor Platt, Shubha Sathyendranath, et Venetia Stuart. 2003. « Bio-optical Properties of the Labrador Sea ». *Journal of Geophysical Research: Oceans* 108(C7):2000JC000597. doi: 10.1029/2000JC000597.

Fick, Dr Adolph. 1855. « V. On Liquid Diffusion ». *The London, Edinburgh, and Dublin Philosophical Magazine and Journal of Science*. doi: 10.1080/14786445508641925.

Franz, Bryan A., Sean W. Bailey, Norman Kuring, et P. Jeremy Werdell. 2015. « Ocean Color Measurements with the Operational Land Imager on Landsat-8: Implementation and

Evaluation in SeaDAS ». *Journal of Applied Remote Sensing* 9(1):096070. doi: 10.1117/1.JRS.9.096070.

Gons, H. J. 2002. « A Chlorophyll-Retrieval Algorithm for Satellite Imagery (Medium Resolution Imaging Spectrometer) of Inland and Coastal Waters ». *Journal of Plankton Research* 24(9):947-51. doi: 10.1093/plankt/24.9.947.

Gons, H. J. 2004. « Effect of a Waveband Shift on Chlorophyll Retrieval from MERIS Imagery of Inland and Coastal Waters ». *Journal of Plankton Research* 27(1):125-27. doi: 10.1093/plankt/fbh151.

Holding, Johnna M., Stiig Markager, Thomas Juul-Pedersen, Maria L. Paulsen, Eva F. Møller, Lorenz Meire, et Mikael K. Sejr. 2019. « Seasonal and Spatial Patterns of Primary Production in a High-Latitude Fjord Affected by Greenland Ice Sheet Run-Off ». *Biogeosciences* 16(19):3777-92. doi: 10.5194/bg-16-3777-2019.

Lewis, K. M., B. G. Mitchell, G. L. Van Dijken, et K. R. Arrigo. 2016. « Regional Chlorophyll a Algorithms in the Arctic Ocean and Their Effect on Satellite-Derived Primary Production Estimates ». *Deep Sea Research Part II: Topical Studies in Oceanography* 130:14-27. doi: 10.1016/j.dsr2.2016.04.020.

Lund-Hansen, Lars Chresten, Thorbjørn Joest Andersen, Morten Holtegaard Nielsen, et Morten Pejrup. 2010. « Suspended Matter, Chl-a, CDOM, Grain Sizes, and Optical Properties in the Arctic Fjord-Type Estuary, Kangerlussuaq, West Greenland During Summer ». *Estuaries and Coasts* 33(6):1442-51. doi: 10.1007/s12237-010-9300-7.

Maciel, F. P., et F. Pedocchi. 2022. « Evaluation of ACOLITE Atmospheric Correction Methods for Landsat-8 and Sentinel-2 in the Río de La Plata Turbid Coastal Waters ». *International Journal of Remote Sensing* 43(1):215-40. doi: 10.1080/01431161.2021.2009149.

MacIntyre, Sally, Anders Jonsson, Mats Jansson, Jan Aberg, Damon E. Turney, et Scott D. Miller. 2010. « Buoyancy Flux, Turbulence, and the Gas Transfer Coefficient in a Stratified Lake ». *Geophysical Research Letters* 37(24). doi: 10.1029/2010GL044164.

Magen, Cédric, Laura L. Lapham, John W. Pohlman, Kathleen Marshall, Samantha Bosman, Michael Casso, et Jeffrey P. Chanton. 2014. « A Simple Headspace Equilibration Method for Measuring Dissolved Methane ». *Limnology and Oceanography: Methods* 12(9):637-50. doi: 10.4319/lom.2014.12.637.

Mascarenhas, Veloisa J., et Oliver Zielinski. 2019. « Hydrography-Driven Optical Domains in the Vaigat-Disko Bay and Godthabsfjord: Effects of Glacial Meltwater Discharge ». *Frontiers in Marine Science* 6:335. doi: 10.3389/fmars.2019.00335.

Matsuoka, Atsushi, Pierre Larouche, Michel Poulin, Warwick Vincent, et Hiroshi Hattori. 2009. « Phytoplankton Community Adaptation to Changing Light Levels in the Southern Beaufort Sea, Canadian Arctic ». *Estuarine, Coastal and Shelf Science* 82(3):537-46. doi: 10.1016/j.ecss.2009.02.024.

McGinnis, D. F., J. Greinert, Y. Artemov, S. E. Beaubien, et A. Wüest. 2006. « Fate of Rising Methane Bubbles in Stratified Waters: How Much Methane Reaches the Atmosphere? » *Journal of Geophysical Research* 111(C9):C09007. doi: 10.1029/2005JC003183.

McGinnis, Daniel F., Georgiy Kirillin, Kam W. Tang, Sabine Flury, Pascal Bodmer, Christof Engelhardt, Peter Casper, et Hans-Peter Grossart. 2015. « Enhancing Surface Methane Fluxes from an Oligotrophic Lake: Exploring the Microbubble Hypothesis ». *Environmental Science & Technology* 49(2):873-80. doi: 10.1021/es503385d.

McGuire, A. David, Leif G. Anderson, Torben R. Christensen, Scott Dallimore, Laodong Guo, Daniel J. Hayes, Martin Heimann, Thomas D. Lorenson, Robie W. Macdonald, et Nigel Roulet. 2009. « Sensitivity of the Carbon Cycle in the Arctic to Climate Change ». *Ecological Monographs* 79(4):523-55. doi: 10.1890/08-2025.1.

Meire, L., D. H. Søgaard, J. Mortensen, F. J. R. Meysman, K. Soetaert, K. E. Arendt, T. Juul-Pedersen, M. E. Blicher, et S. Rysgaard. 2015a. « Glacial Meltwater and Primary Production Are Drivers of Strong CO2 Uptake in Fjord and Coastal Waters Adjacent to the Greenland Ice Sheet ». *Biogeosciences* 12(8):2347-63. doi: 10.5194/bg-12-2347-2015.

Meire, L., D. H. Søgaard, J. Mortensen, F. J. R. Meysman, K. Soetaert, K. E. Arendt, T. Juul-Pedersen, M. E. Blicher, et S. Rysgaard. 2015b. « Glacial Meltwater and Primary Production Are Drivers of Strong CO2 Uptake in Fjord and Coastal Waters Adjacent to the Greenland Ice Sheet ». *Biogeosciences* 12(8):2347-63. doi: 10.5194/bg-12-2347-2015.

Morel, André, Yannick Huot, Bernard Gentili, P. Jeremy Werdell, Stanford B. Hooker, et Bryan A. Franz. 2007. « Examining the Consistency of Products Derived from Various Ocean Color Sensors in Open Ocean (Case 1) Waters in the Perspective of a Multi-Sensor Approach ». *Remote Sensing of Environment* 111(1):69-88. doi: 10.1016/j.rse.2007.03.012.

Murray, Ciarán, Stiig Markager, Colin A. Stedmon, Thomas Juul-Pedersen, Mikael K. Sejr, et Annette Bruhn. 2015. « The Influence of Glacial Melt Water on Bio-Optical Properties in Two Contrasting Greenlandic Fjords ». *Estuarine, Coastal and Shelf Science* 163:72-83. doi: 10.1016/j.ecss.2015.05.041.

Nakaoka, Shin-Ichiro, Shuji Aoki, Takakiyo Nakazawa, Gen Hashida, Shinji Morimoto, Takashi Yamanouchi, et Hisayuki Yoshikawa-Inoue. 2006. « Temporal and Spatial Variations of Oceanic PCO_2 and Air–Sea CO_2 Flux in the Greenland Sea and the Barents Sea ». *Tellus B: Chemical and Physical Meteorology* 58(2):148. doi: 10.1111/j.1600-0889.2006.00178.x.

O'Reilly, John E., Stéphane Maritorena, B. Greg Mitchell, David A. Siegel, Kendall L. Carder, Sara A. Garver, Mati Kahru, et Charles McClain. 1998. « Ocean Color Chlorophyll Algorithms for SeaWiFS ». *Journal of Geophysical Research: Oceans* 103(C11):24937-53. doi: 10.1029/98JC02160.

O'Reilly, John E., Stephane Maritorena, David A. Siegel, Margaret C. O'Brien, Dierdre Toole, B. Greg Mitchell, Mati Kahru, Francisco P. Chavez, P. Strutton, Glenn F. Cota,

Stanford B. Hooker, Charles R. McClain, Kendall L. Carder, Frank Muller-Karger, Larry Harding, Andrea Magnuson, David Phinney, Gerald F. Moore, James Aiken, Kevin R. Arrigo, Ricardo Letelier, et Mary Culver. 2000. « Ocean Color Chlorophyll a Algorithms for SeaWiFS, OC2 and OC4: Version 4 ».

O'Reilly, John E., et P. Jeremy Werdell. 2019. « Chlorophyll Algorithms for Ocean Color Sensors - OC4, OC5 & OC6 ». *Remote Sensing of Environment* 229:32-47. doi: 10.1016/j.rse.2019.04.021.

Pahlevan, Nima, Antoine Mangin, Sundarabalan V. Balasubramanian, Brandon Smith, Krista Alikas, Kohei Arai, Claudio Barbosa, Simon Bélanger, Caren Binding, Mariano Bresciani, Claudia Giardino, Daniela Gurlin, Yongzhen Fan, Tristan Harmel, Peter Hunter, Joji Ishikaza, Susanne Kratzer, Moritz K. Lehmann, Martin Ligi, Ronghua Ma, François-Régis Martin-Lauzer, Leif Olmanson, Natascha Oppelt, Yanqun Pan, Steef Peters, Nathalie Reynaud, Lino A. Sander De Carvalho, Stefan Simis, Evangelos Spyrakos, François Steinmetz, Kerstin Stelzer, Sindy Sterckx, Thierry Tormos, Andrew Tyler, Quinten Vanhellemont, et Mark Warren. 2021. « ACIX-Aqua: A Global Assessment of Atmospheric Correction Methods for Landsat-8 and Sentinel-2 over Lakes, Rivers, and Coastal Waters ». *Remote Sensing of Environment* 258:112366. doi: 10.1016/j.rse.2021.112366.

Pahlevan, Nima, Brandon Smith, John Schalles, Caren Binding, Zhigang Cao, Ronghua Ma, Krista Alikas, Kersti Kangro, Daniela Gurlin, Nguyễn Hà, Bunkei Matsushita, Wesley Moses, Steven Greb, Moritz K. Lehmann, Michael Ondrusek, Natascha Oppelt, et Richard Stumpf. 2020. « Seamless Retrievals of Chlorophyll-a from Sentinel-2 (MSI) and Sentinel-3 (OLCI) in Inland and Coastal Waters: A Machine-Learning Approach ». *Remote Sensing of Environment* 240:111604. doi: 10.1016/j.rse.2019.111604.

Parmentier, Frans-Jan W., Torben R. Christensen, Lise Lotte Sørensen, Søren Rysgaard, A. David McGuire, Paul A. Miller, et Donald A. Walker. 2013. « The Impact of Lower Sea-Ice Extent on Arctic Greenhouse-Gas Exchange ». *Nature Climate Change* 3(3):195-202. doi: 10.1038/nclimate1784.

Royal Belgian Institute of Natural Sciences (RBINS). 2023. « ACOLITE User Manual edition 23.10.2023 ».

Ruiz-Halpern, Sergio, Mikael K. Sejr, Carlos M. Duarte, Dorte Krause-Jensen, Tage Dalsgaard, Jordi Dachs, et Søren Rysgaard. 2010. « Air-Water Exchange and Vertical Profiles of Organic Carbon in a Subarctic Fjord ». *Limnology and Oceanography* 55(4):1733-40. doi: 10.4319/lo.2010.55.4.1733.

Rysgaard, S., J. Mortensen, T. Juul-Pedersen, L. L. Sørensen, K. Lennert, D. H. Søgaard, K. E. Arendt, M. E. Blicher, M. K. Sejr, et J. Bendtsen. 2012. « High Air–Sea CO2 Uptake Rates in Nearshore and Shelf Areas of Southern Greenland: Temporal and Spatial Variability ». *Marine Chemistry* 128-129:26-33. doi: 10.1016/j.marchem.2011.11.002.

Sander, Rolf. 2023. « Compilation of Henry's Law Constants (Version 5.0.0) for Water as Solvent ». *Atmospheric Chemistry and Physics* 23(19):10901-440. doi: 10.5194/acp-23-10901-2023.

Saunois, Marielle, Ann R. Stavert, Ben Poulter, Philippe Bousquet, Josep G. Canadell, Robert B. Jackson, Peter A. Raymond, Edward J. Dlugokencky, Sander Houweling, Prabir K. Patra, Philippe Ciais, Vivek K. Arora, David Bastviken, Peter Bergamaschi, Donald R. Blake, Gordon Brailsford, Lori Bruhwiler, Kimberly M. Carlson, Mark Carrol, Simona Castaldi, Naveen Chandra, Cyril Crevoisier, Patrick M. Crill, Kristofer Covey, Charles L. Curry, Giuseppe Etiope, Christian Frankenberg, Nicola Gedney, Michaela I. Hegglin, Lena Höglund-Isaksson, Gustaf Hugelius, Misa Ishizawa, Akihiko Ito, Greet Janssens-Maenhout, Katherine M. Jensen, Fortunat Joos, Thomas Kleinen, Paul B. Krummel, Ray L. Langenfelds, Goulven G. Laruelle, Licheng Liu, Toshinobu Machida, Shamil Maksyutov, Kyle C. McDonald, Joe McNorton, Paul A. Miller, Joe R. Melton, Isamu Morino, Jurek Müller, Fabiola Murguia-Flores, Vaishali Naik, Yosuke Niwa, Sergio Noce, Simon O'Doherty, Robert J. Parker, Changhui Peng, Shushi Peng, Glen P. Peters, Catherine Prigent, Ronald Prinn, Michel Ramonet, Pierre Regnier, William J. Riley, Judith A. Rosentreter, Arjo Segers, Isobel J. Simpson, Hao Shi, Steven J. Smith, L. Paul Steele, Brett F. Thornton, Hanqin Tian, Yasunori Tohjima, Francesco N. Tubiello, Aki Tsuruta, Nicolas Viovy, Apostolos Voulgarakis, Thomas S. Weber, Michiel van Weele, Guido R. van der Werf, Ray F. Weiss, Doug Worthy, Debra Wunch, Yi Yin, Yukio Yoshida, Wenxin Zhang, Zhen Zhang, Yuanhong Zhao, Bo Zheng, Qing Zhu, Qiuan Zhu, et Qianlai Zhuang. 2020. « The Global Methane Budget 2000–2017 ». *Earth System Science Data* 12(3):1561-1623. doi: 10.5194/essd-12-1561-2020.

Sejr, M. K., D. Krause-Jensen, S. Rysgaard, L. L. Sørensen, P. B. Christensen, et R. N. Glud. 2011. « Air–Sea Flux of CO_2 in Arctic Coastal Waters Influenced by Glacial Melt Water and Sea Ice ». *Tellus B: Chemical and Physical Meteorology* 63(5):815. doi: 10.1111/j.1600-0889.2011.00540.x.

Straneo, Fiamma, et Claudia Cenedese. 2015. « The Dynamics of Greenland's Glacial Fjords and Their Role in Climate ». *Annual Review of Marine Science* 7(1):89-112. doi: 10.1146/annurev-marine-010213-135133.

Tehrani, Nadia Abbaszadeh, Milad Janalipour, et Hadiseh Babaei. 2021. « Estimating Water Surface Chlorophyll-a Concentration by Big Remote Sensing Data in the Persian Gulf, Bushehr ». *Remote Sensing in Earth Systems Sciences* 4(1-2):87-95. doi: 10.1007/s41976-021-00045-2.

Tilstone, Gavin H., Silvia Pardo, Giorgio Dall'Olmo, Robert J. W. Brewin, Francesco Nencioli, David Dessailly, Ewa Kwiatkowska, Tania Casal, et Craig Donlon. 2021. « Performance of Ocean Colour Chlorophyll a Algorithms for Sentinel-3 OLCI, MODIS-Aqua and Suomi-VIIRS in Open-Ocean Waters of the Atlantic ». *Remote Sensing of Environment* 260:112444. doi: 10.1016/j.rse.2021.112444.

Vanhellemont, Quinten, et Kevin Ruddick. 2016. « ACOLITE FOR SENTINEL-2: AQUATIC APPLICATIONS OF MSI IMAGERY ».

Vanhellemont, Quinten, et Kevin Ruddick. 2018. « Atmospheric Correction of Metre-Scale Optical Satellite Data for Inland and Coastal Water Applications ». *Remote Sensing of Environment* 216:586-97. doi: 10.1016/j.rse.2018.07.015.

Von Schneidemesser, Erika, James J. Schauer, Gayle S. W. Hagler, et Michael H. Bergin. 2009. « Concentrations and Sources of Carbonaceous Aerosol in the Atmosphere of

Summit, Greenland ». *Atmospheric Environment* 43(27):4155-62. doi: 10.1016/j.atmosenv.2009.05.043.

Wanninkhof, Rik. 2014. « Relationship between Wind Speed and Gas Exchange over the Ocean Revisited: Gas Exchange and Wind Speed over the Ocean ». *Limnology and Oceanography: Methods* 12(6):351-62. doi: 10.4319/lom.2014.12.351.

Weber, Thomas, Nicola A. Wiseman, et Annette Kock. 2019. « Global Ocean Methane Emissions Dominated by Shallow Coastal Waters ». *Nature Communications* 10(1):4584. doi: 10.1038/s41467-019-12541-7.

Zhou, Y. T., Q. Shen, H. C. Peng, Y. Yao, R. Wang, W. Y. Ma, J. R. Shi, Y. J. Ren, J. Zhao, W. T. Xu, L. Hao, et Z. J. Zhang. 2023. « Suitability of Sentinel-3 Chlorophyll a Products Based on Optical Water Types ». *International Journal of Remote Sensing* 44(4):1369-89. doi: 10.1080/01431161.2023.2180780.

Zhu, Xiaotong, Hongwei Guo, Jinhui Jeanne Huang, Shang Tian, Wang Xu, et Youquan Mai. 2022. « An Ensemble Machine Learning Model for Water Quality Estimation in Coastal Area Based on Remote Sensing Imagery ». *Journal of Environmental Management* 323:116187. doi: 10.1016/j.jenvman.2022.116187.

Appendixes

Appendix 1. Description of the sampling and post-processing leading to the acquisition of the GHGs dataset.

Sampling:

The data collected is aimed at obtaining the concentrations of CO_2 and CH_4 in the air, as well as in the arctic water, to estimate the sea-air fluxes.

Both atmospheric and oceanographic samples were taken manually on starboard side of a boat to quantify CO_2 and CH_4 concentrations. A minimum of 2 samples per day were established, however this depended on local weather and sailing conditions. A CTD (YSI EXO2 Multiparameter Sonde) was installed through the hull of the ship, just below the surface so it always remained in the water. This instrument collected surface water temperature [°C], salinity [PSU], depth of the sonde [m], atmospheric pressure [mbar] and dissolved oxygen [% sat], with a 10-minute interval.

The manual measurements of the atmospheric concentration were performed with a 30 [ml] syringe. Air was taken at a height above the body, in order not to contaminate the air sample with breath. It was then directly introduced into a 10 [ml] exetainer.

For surface water, the headspace method was used which equilibrates the gas molecules in the aqueous phase and those in the gaseous phase. A hose system was installed next to the CTD borehole to take water samples. In this way, the samples of water collected corresponded to the CTD measurements. Two samples of water were performed per point of sampling. Using a 140 [ml] syringe, water was taken through the hose. Then, the air bubbles were removed, along with 35 [ml] of water to create the headspace, that was then filled with atmospheric air. To equilibrate the molecules, the syringe were shaken for 2 minutes (Magen et al. 2014). The air on the top was then transferred to a 30 [ml] dry syringe and then introduced into a 10 [ml] exetainer.

Post-processing:

All the exetainers resulting from the sampling were taken to the Aquatic Physic laboratory at the University of Geneva to be treated with the Picarro Gas Concentration and Isotope Analyzer (Picarro G2201-i, Picarro, CA, USA). This instrument allows high precision in CO_2 and CH_4 concentration measurements. To automate the process, a SAM auto-sampler was used.[7]

Appendix 2 describes all the procedures and equations that were used to calculate the flux of CO_2 and CH_4 from the ocean to the atmosphere at the air-water interface.

[7] Openautosampler, https://www.openautosampler.com/

Appendix 2. Description of the sampling and post-processing leading to the acquisition of the GHGs dataset.

To calculate	Equation		
Gas concentration in the headspace	Ideal Gas Law (Magen et al. 2014)	$n = \frac{Pi * V}{R * T}$	n, number of moles, Pi, partial pressure [Pa], V, volume [m3], R, the ideal gas constant [J $K^{-1}mol^{-1}$] T, temperature [K].
Dissolved water concentration	Henry's Law (Sander 2023)	$Ceq = Hi * Pi$	Ceq, solubility of the gas [mmol m^{-3}], Hi, Henry's coefficient, Pi, the partial pressure [Pa].
Gas transfer velocity - K600	Gas transfer velocity (MacIntyre et al. 2010)	$K600 = 2.04 * u10 + 2.0$	u, wind speed
Schmit number - Sc	Schmit number (Wanninkhof 2014)	$ScCH_4 = 2039.2 - 120.31t + 3.4209\ t^2 - 0.040437t^3$ $ScCO_2 = 2073.1 - 125.62t + 3.6276t^2 - 0.043219t^3$	t, water temperature
Exchange coefficient - Ki	Gas exchange (McGinnis et al. 2015)	$Ki = K600 * (600/Sc)^{-n}$	K600 [m s^{-1}] is the gas transfer velocity. Sc, Schmit number For the wind, n: n = 0.5 for wind speeds > 3.7 [m s^{-1}] or, n = 0.66 for wind speeds < 3.7 [m s^{-1}]
Flux from the ocean to the atmosphere at the sea-air interface	Fick's first law (Fick 1855)	$Fgas = Ki * (Cw - Ceq)$	Fgas, flux of gas [mmol m^{-2} d^{-1}] for the CO_2 and in [µmol m^{-2} d^{-1}] for the CH_4. Ki, exchange coefficient [m d^{-1}]. Cw, concentration of dissolved gas in water, Ceq, concentration at equilibrium [mmol m^{-3}].

Appendix 3. Table of data removed during the post-processing of the data.

Samples name	Problem	Modification
MAU210707 B	Atmospheric CO_2 [ppm] too high	Removed
MAU210707 E	Wrong coordinates	Removed
MAU210707 F	Wrong coordinates	Removed
MAU210707 H	Atmospheric CH_4 [ppm] very low	Removed
MAU210712 A	Atmospheric CH_4 [ppm] very low	Removed
MAU210712 B	Atmospheric CH_4 [ppm] very low	Removed
MAU210725 C	Atmospheric CH_4 [ppm] too high, with negative dissolved CH_4 concentrations	Removed
MAU210725 D	Atmospheric CH_4 [ppm] too high, with negative dissolved CH_4 concentrations	Removed
MAU210725 K	Wrong coordinates	Removed
MAU210725 L	Wrong coordinates	Removed
MAU210726 D	Contamination from a nearby CO_2 source	Removed
MAU210726 E	Contamination from a nearby CO_2 source	Removed
MAU210726 J	Contamination from a nearby CO_2 source	Removed
MAU210726 G	Atmospheric CH_4 [ppm] too high, with negative dissolved CH_4 concentrations	Removed
MAU210726 H	Atmospheric CH_4 [ppm] too high, with negative dissolved CH_4 concentrations	Removed
MAU210726 I	Atmospheric CH_4 [ppm] too high, with negative dissolved CH_4 concentrations	Removed
MAU220806 A	Atmospheric CO_2 [ppm] too high	Removed
MAU220806 B	Wrong coordinates	Removed

Appendix 4. Average and standard deviation of all pixels from the four different algorithms for the 9th of July 2021 (8th of July for the OC4Me).

Algorithm	Mean	Std. Dev.
OC3 (Pahlevan et al. 2020)	1	0.95
OC3L (derived from Cota 2004)	1.41	2.12
Red-edge (Gons 2004)	17.79	13.24
OC4Me (Morel et al. 2007)	5.03	10.25

Appendix 5. Average and standard deviation of all pixels from the four different algorithms for the 29th of July 2021 (28th of July for the OC4Me).

Algorithm	Mean	Std. Dev.
OC3 (Pahlevan et al. 2020)	1.19	1.59
OC3L (derived from Cota 2004)	1.84	3.18
Red-edge (Gons 2004)	15.7	12.15
OC4Me (Morel et al. 2007)	4.48	10.88

Appendix 6. Scatterplot of red-edge and OC3L Chl-a estimates in [mg m^{-3}] for the 22nd of June 2021.

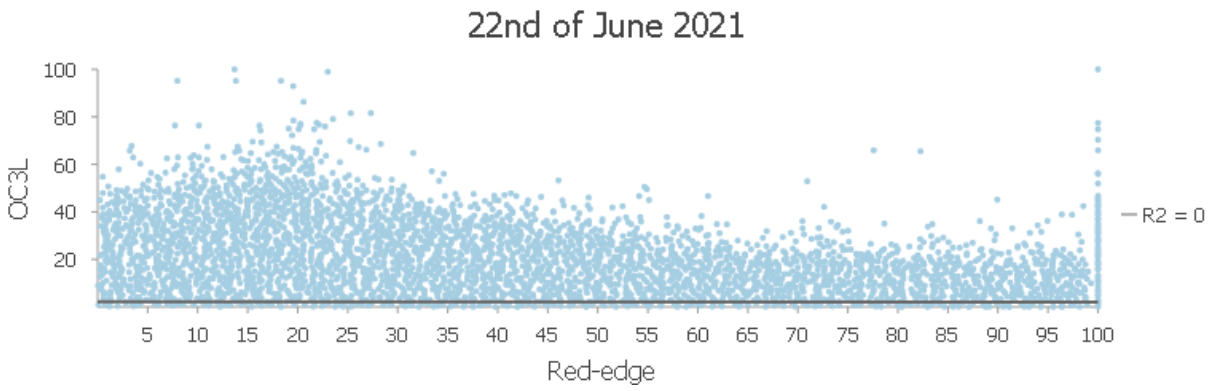

Appendix 7. Scatterplot of red-edge and OC3L Chl-a estimates in [mg m^{-3}] for the 9th of July 2021.

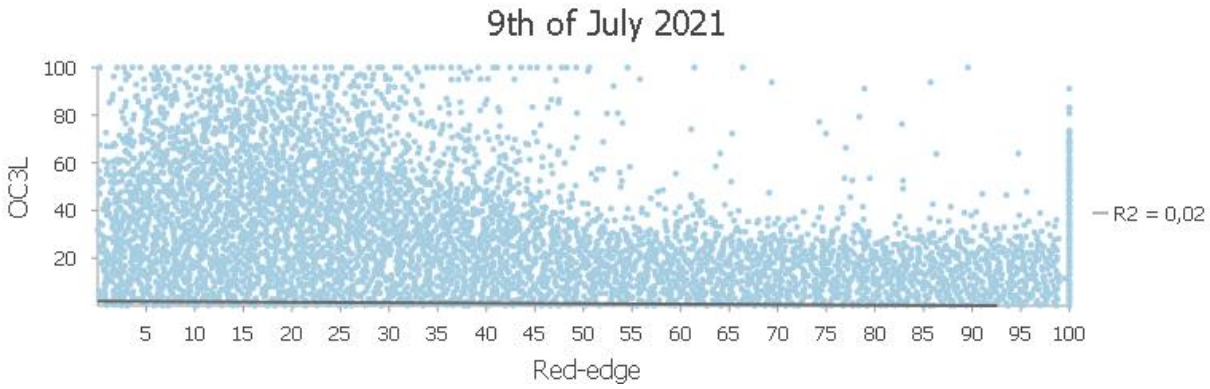

Appendix 8. Scatterplot of red-edge and OC3L Chl-a estimates in [mg m^{-3}] for the 29th of July 2021.

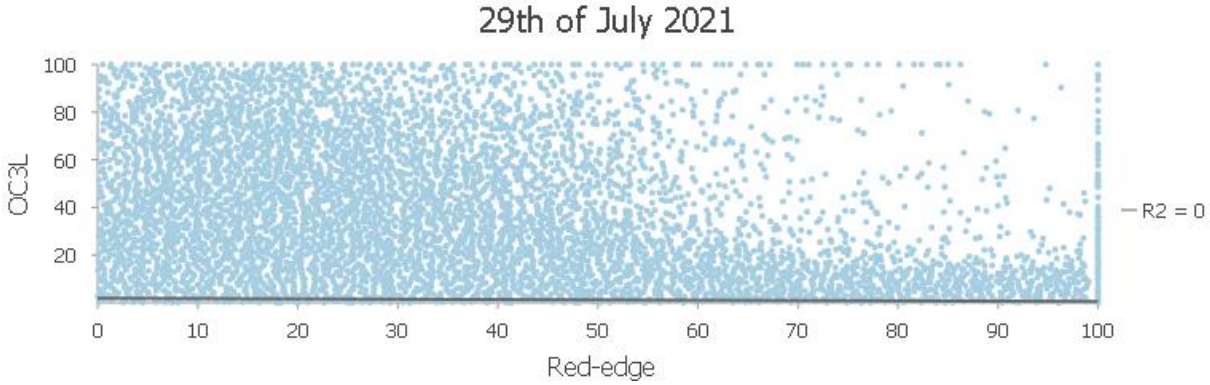

Appendix 9. Scatterplot of OC3 and OC3L Chl-a estimates in [mg m^{-3}] for the 22nd of June 2021.

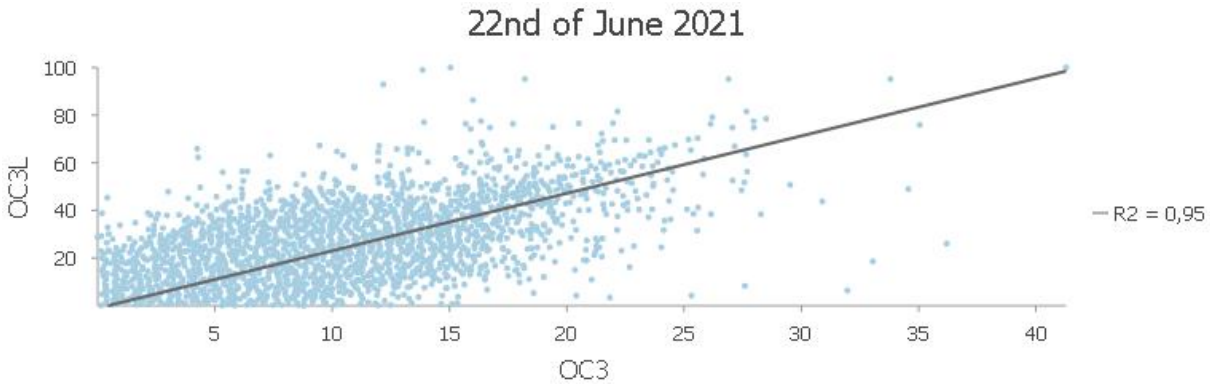

Appendix 10. Scatterplot of OC3 and OC3L Chl-a estimates in [mg m^{-3}] for the 9th of July 2021.

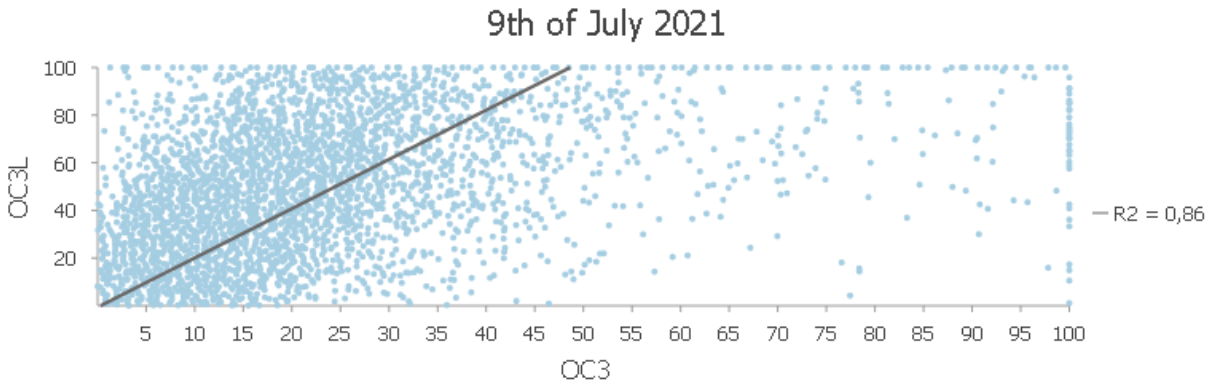

Appendix 11. Scatterplot of OC3 and OC3L Chl-a estimates in [mg m^{-3}] for the 29th of July 2021.

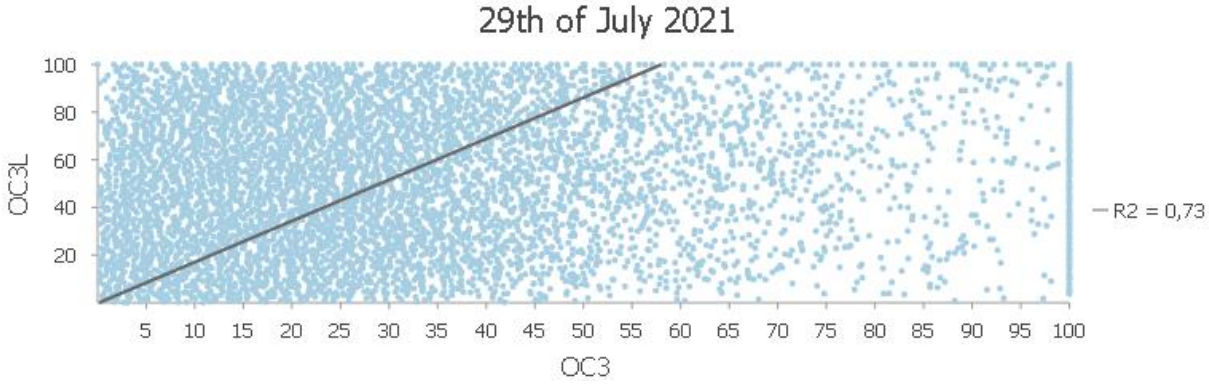

.

Appendix 12. Difference OC3L – OC3 in [mg m^{-3}] for the 9th of July 2021. Positive values are when OC3L > OC3.

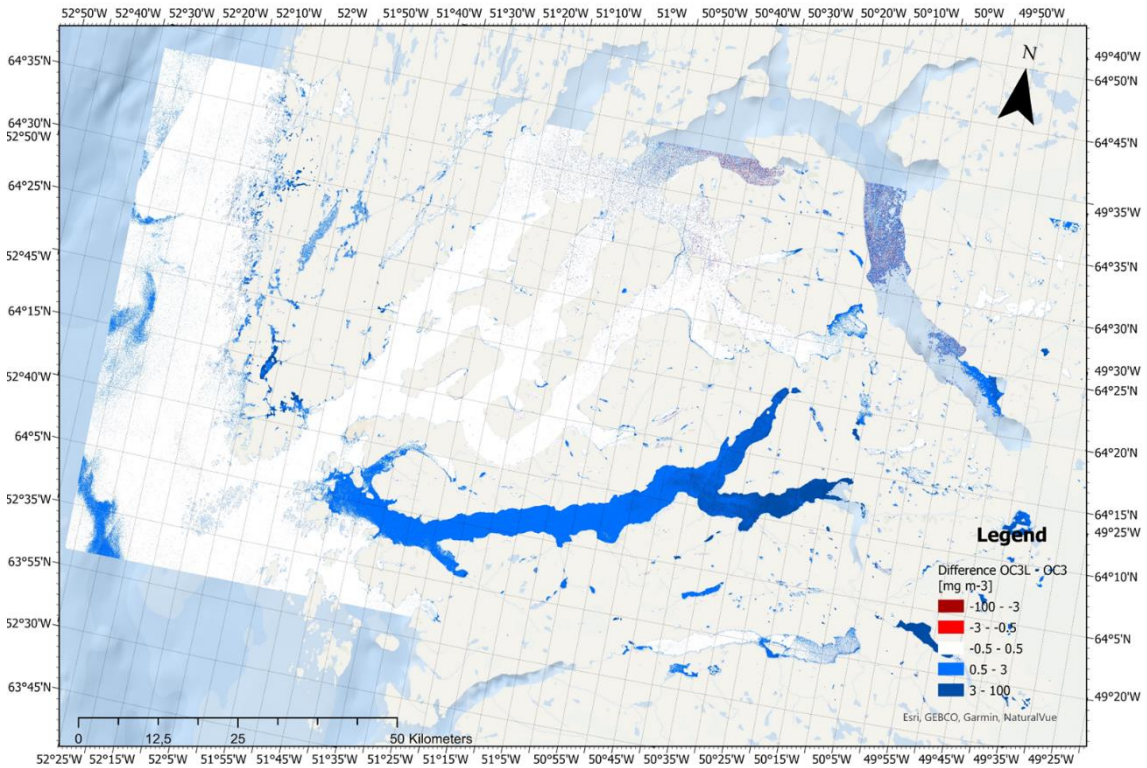

Appendix 13. Difference OC3L – OC3 in [mg m^{-3}] for the 29th of July 2021. Positive values are when OC3L > OC3.

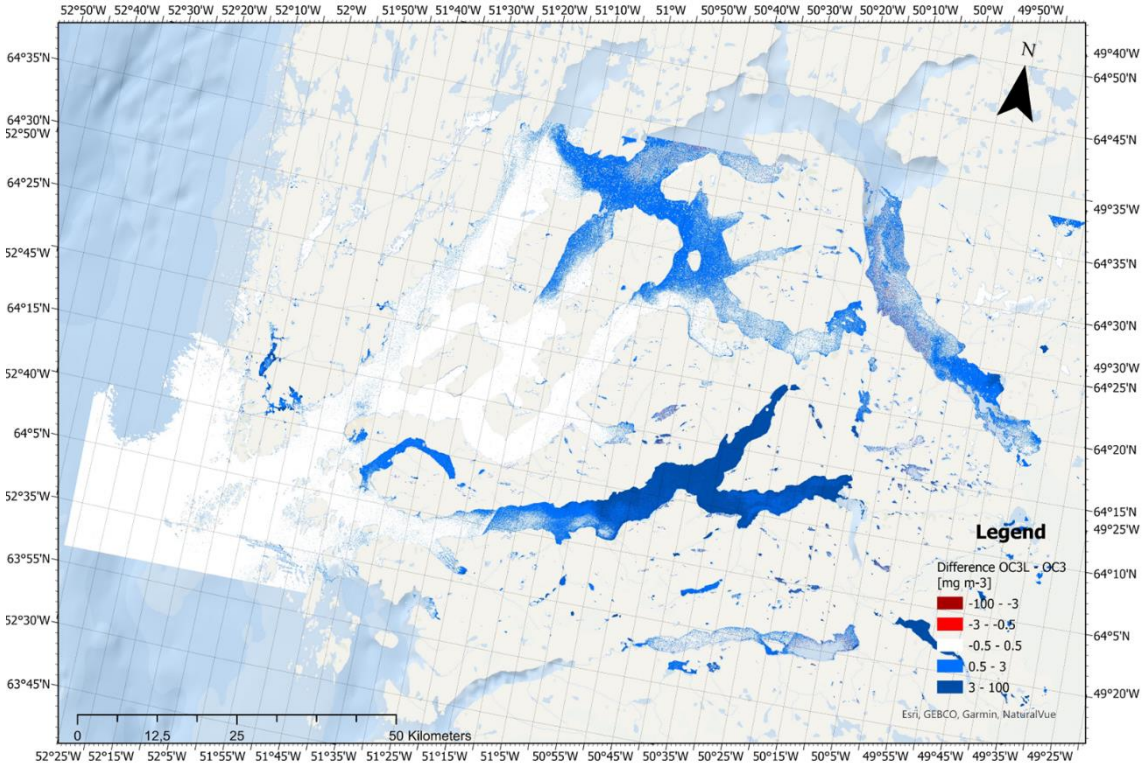

Appendix 14. Difference OC3L – OC4Me in [mg m^{-3}] for the 8-9th of July 2021. Positive values are when OC3L > OC4Me.

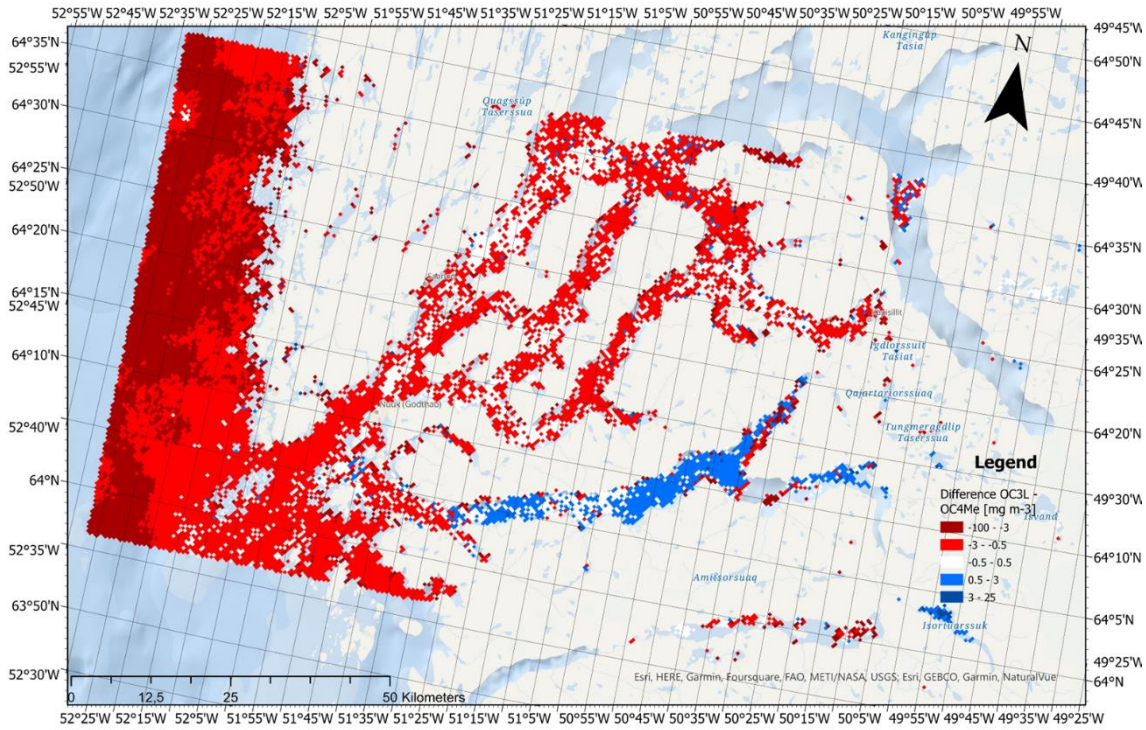

Appendix 15. Difference OC3L – OC4Me in [mg m^{-3}] for the 28-29th of July 2021. Positive values are when OC3L > OC4Me.

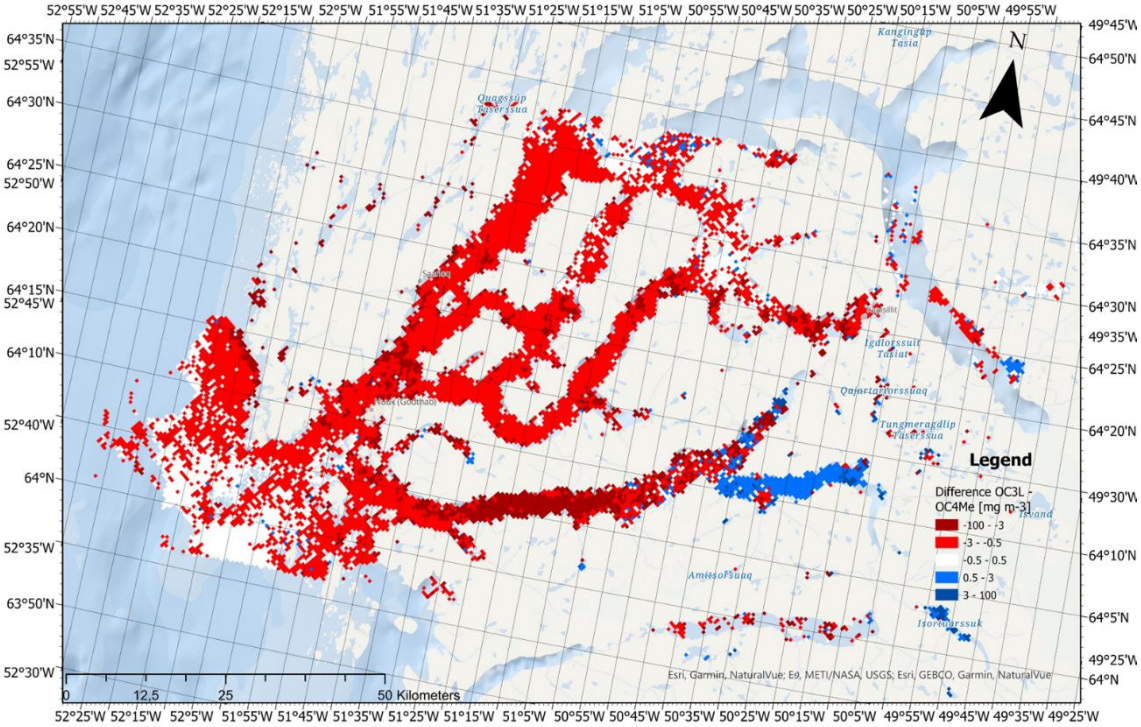

Appendix 16. Average and standard deviation of CO_2 and CH_4 fluxes in regard of two categories, above 2 [mg m^{-3}] of Chl-a ("High Chl-a") or below ("Low Chl-a").

	CO_2 sea-air fluxes [mmol m^{-2} d^{-1}]		**CH_4 sea-air fluxes [µmol m^{-2} d^{-1}]**	
	Mean	**Std. Dev.**	**Mean**	**Std. Dev.**
High Chl-a	-16.29	20.34	30.14	34.98
Low Chl-a	-18.5	16.73	9.35	7.34
Total	-17.65	17.42	14.67	19.74

Appendix 17. Average and standard deviation of CO_2 dissolved concentrations and fluxes for the two water types identified with Figure 7.

Water Type	**Dissolved CO_2 concentrations [ppm]**		**CO_2 sea-air fluxes [mmol m^{-2} d^{-1}]**	
	Mean	**Std. Dev.**	**Mean**	**Std. Dev.**
Nuup Kangerlua water	273.48	88.73	-28.88	18.97
Baffin Bay water	383.72	69.48	-11.23	12.66
Total	343.64	93.36	-17.65	17.42

Appendix 18. From (Bonaglia et al. 2022). *Surface methane concentrations and methane emissions to the atmosphere across 10 fjords worldwide. The average flux is the average of all average emissions ± standard error.*

Basin	Fjord name (country)	CH_4 concentration Range, nM	CH_4 emission Range (average), μmol m^{-2} d^{-1}	Observation number and season	Method	Reference
Skagerrak Sea	By Fjord (Sweden)	43–418	17–641 (193)	$n = 14$, year-round	Headspace + GC	This study
Kattegat Sea	Randers Fjord (Denmark)	28–420	23–420 (229)	$n = 37$, year-round	Headspace + GC	Abril and Iversen (2002)
Kattegat Sea	Mariager Fjord (Denmark)	500–900	190–4980 (3080)	$n = 6$, summer	Chambers + GC	Fenchel et al. (1995)
Pacific Ocean	Reloncaví Fjord (Chile)	17–151	24–136 (80)	$n = 14$, winter	Headspace + GC	Farías et al. (2017)
Pacific Ocean	Concepción Channel (Chile)	4–7	−2 to 10 (3)	$n = 4$, spring	Headspace + GC	Farías et al. (2018)
Pacific Ocean	Peel Fjord (Chile)	3–9	0–2 (1)	$n = 3$, spring	Headspace + GC	Farías et al. (2018)
Pacific Ocean	Última Esperanza Sound (Chile)	17–151	−1 to 4 (2)	$n = 4$, spring	Headspace + GC	Farías et al. (2018)
Pacific Ocean	Smyth Channel (Chile)	17–151	16–64 (46)	$n = 3$, spring	Headspace + GC	Farías et al. (2018)
Pacific Ocean	Saanich Inlet (Canada)	8–145	2–18 (7)	$n = 22$, year-round	Headspace + GC-IRMS	Capelle et al. (2019)
Atlantic Ocean	Saguenay Fjord (Canada)	16–184	16–257 (53)	$n = 27$, fall and summer	Headspace + GC	Li et al. (2021)
Average flux			369			
Standard error			302			